

¹ A novel inf–sup–based volumetric constraint ratio and
² its implementation via mixed FE-meshfree formulation

³ Junchao Wu^{a,*}, Yingjie Chu^b, Yangtao Xu^a

^a Key Laboratory for Intelligent Infrastructure and Monitoring of Fujian Province, College
of Civil Engineering, Huaqiao University , Xiamen, Fujian, 361021, China

^b Fujian Key Laboratory of Digital Simulations for Coastal Civil Engineering, Department
of Civil Engineering, Xiamen University , Xiamen, Fujian, 361005, China

⁴ **Abstract**

Numerical formulations for incompressible materials often suffer from volumetric locking, which reduces the accuracy of displacement solutions and introduces oscillations in the pressure field. A well-chosen constraint ratio can mitigate this issue, but traditional approaches lack a theoretical foundation based on the inf–sup (or LBB) condition, which is essential for the stability of mixed formulations. This paper introduces a novel optimal constraint ratio derived from the inf–sup condition to address volumetric locking. The inf–sup test, a numerical tool for verifying the inf–sup condition, is reaffirmed to be equivalent to the inf–sup condition through a variational approach. By incorporating a complete polynomial space whose dimension matches the number of displacement degrees of freedom (DOFs), a new inf–sup value estimator is developed, explicitly considering the constraint ratio. For a given number of displacement DOFs, when the pressure DOFs of a numerical formulation remain below a stabilized number that falls into the optimal constraint ratio range, this numerical formulation actually satisfies the inf–sup condition. To implement the optimal constraint ratio, a mixed finite element and meshfree formulation is proposed, where displacements are discretized using traditional finite element approximations, and pressures are approximated via the reproducing kernel meshfree method. Leveraging the globally smooth reproducing kernel shape functions, the constraint ratio can be flexibly adjusted to meet the inf–sup condition without the limit of element. For computational efficiency and ease of implementation, pressure nodes are placed on selected displacement nodes to maintain the optimal constraint ratio. Inf–sup tests and a series of 2D and 3D incompressible elasticity examples validate the proposed constraint ratio, demonstrating its effectiveness in eliminating volumetric locking and enhancing the performance of mixed finite element and meshfree formulations.

⁵ **Keywords:** Optimal constraint ratio, Inf–sup condition estimator, Volumetric
⁶ locking, Mixed formulation, Reproducing kernel meshfree approximation

*Corresponding author

Email address: jcwu@hqu.edu.cn (Junchao Wu)

7 **1. Introduction**

8 The volumetric constraint is a necessary condition in the numerical formulation
 9 of incompressible materials like rubber and hydrogel. Proper imposition of
 10 this constraint is crucial for obtaining better numerical solutions; insufficient or
 11 excessive constraints will reduce the accuracy and stability of the solution [1].
 12 The volumetric constraint ratio [2], denoted as r , is often used to measure the
 13 level of constraint. It is defined as the total degrees of freedom (DOFs) of dis-
 14 placement divided by the total DOFs of pressure. Ideally, the optimal constraint
 15 ratio should be consistent with its governing partial differential equations. For
 16 example, in the two-dimensional (2D) case, the optimal constraint ratio is 2,
 17 since there are two governing equations for displacement and one for pressure.
 18 When the constraint ratio is less than 2, the formulation suffers from volumetric
 19 locking, while a constraint ratio greater than 2 can cause a coarse solution for
 20 pressure. These observations have been summarized as follows[2]:

$$r = \frac{2n_u}{n_p}, \quad \begin{cases} r > 2 & \text{too few constraints} \\ r = 2 & \text{optimal} \\ r < 2 & \text{too many constraints} \\ r \leq 1 & \text{severe locking} \end{cases} \quad (1)$$

21 where n_u and n_p are the numbers of control nodes for displacement and pressure,
 22 respectively. Classifying the locked status via the constraint ratio is straight-
 23 forward but imprecise. For instance, the constraint ratio can remain 2 while
 24 the pressure is discretized using continuous shape functions identical to the
 25 displacement's approximation. However, volumetric locking still exists in this
 26 formulation [2].

27 The inf-sup condition, also known as the Ladyzhenskay–Babuka–Brezzi
 28 (LBB) condition [3, 4], is a more precise requirement for a locking-free for-
 29 mulation. This condition is based on the mixed formulation framework, and
 30 when the inf-sup condition is satisfied, both the accuracy and stability of the
 31 mixed-formulation can be ensured. However, verifying the inf-sup condition is
 32 non-trivial. An eigenvalue problem namely inf-sup test can be used to check
 33 this condition numerically [5, 6, 7, 8]. Analytically, Brezzi and Fortin proposed
 34 a two-level projection framework that always satisfies the inf-sup condition, al-
 35 lowing it to be checked by identifying whether the formulation is included in
 36 this framework. Both analytical and numerical methods to check the inf-sup
 37 condition are complex, and the relationship between the constraint ratio and
 38 the inf-sup condition remains unclear.

39 To address volumetric constraint issues, adjusting the constraint ratio to an
 40 appropriate level is commonly used and easily implemented. In traditional finite
 41 element methods (FEM), this adjustment is carried out based on elements since
 42 the DOFs are embedded in each element. Conventional FEM often exhibits
 43 an over-constrained status. Reducing the approximation order of pressure in
 44 mixed formulation can alleviate the constraint burden, such as with the well-
 45 known Q4P1 (4-node quadrilateral displacement element with 1-node piecewise

constant pressure element) and Q8P3. Globally, using continuous shape functions to link the local pressure DOFs in each element can also reduce the total number of pressure DOFs and increase the constraint ratio, such as with T6C3 (6-node triangular displacement element with 3-node continuous linear pressure element) and Q9C4 (Taylor–Hood element) [9]. These schemes belong to the mixed formulation framework and can also be implemented through a projection approach, where the pressure approximant is projected into a lower-dimensional space. Examples include selective integration methods [10, 11], B–bar or F–bar methods [12, 13, 14, 15], pressure projection methods [16, 17, 18, 19, 20], and enhanced strain method [21]. Meanwhile, conventional 3-node triangular elements arranged in a regular cross pattern can also reduce the dimension of the pressure space [22]. It should be noted that not all of these methods meet the inf–sup condition despite alleviating volumetric locking and producing a good displacement solution. Some methods, like Q4P1, show significant oscillation for the pressure solution, known as spurious pressure mode or checkerboard mode [22]. In such cases, additional stabilization approaches, such as variational multi-scale stabilization (VMS) [23, 24, 25, 26, 27], Galerkin/least-squares (GLS) [28], or Streamline upwind/Petrov–Galerkin formulation (SUPG) [29, 30] are required to eliminate the oscillations in pressure.

Another class of FEM methods adjusts the constraint ratio by increasing the displacement DOFs. For instance, based on 3-node triangular elements, Arnold et al. [31, 32] used a cubic bubble function in each element to increase the displacement DOFs, known as the MINI element. It has been shown that this method belongs to the VMS framework [33], and its fulfillment of the inf–sup condition can be analytically evidenced using the two-level projection framework [7]. The Crouzeix–Raviart element [34] transfers the DOFs from the triangular vertices to edges, increasing the constraint ratio since, for triangular topology, the number of edges is greater than that of vertices. More details about FEM technology for volumetric constraint issues can be found in Refs. [2, 4, 35].

In the past two decades, various novel approximations equipped with globally smooth shape functions, such as moving least-squares approximation [36], reproducing kernel approximation [37, 38], radial basis functions [39, 40], maximum-entropy approximation [41], and NURBS approximation [42, 43], have been proposed. In these approaches, the approximant pressure evaluated by the derivatives of globally continuous shape functions also maintains a constraint ratio of 2 in 2D incompressible elasticity problems. However, the corresponding results still show lower accuracy caused by locking [44, 45]. Widely-used locking-free technologies for FEM are introduced in these approaches to enhance their performance. For example, Moutsanidis et al. [46, 47] employed selective integration and B–bar, F–bar methods for reproducing kernel particle methods. Wang et al. [48] applied selective integration schemes with bubble-stabilized functions to node-based smoothed particle FEM. Elguedj et al. [49] proposed the B–bar and F–bar NURBS formulations for linear and nonlinear incompressible elasticity. Chen et al. [50] adopted the pressure projection approach for reproducing kernel formulations for nearly-incompressible problems, which was later extended

to Stokes flow formulations by Goh et al. [51]. Bombarde et al. [52] developed a block-wise NURBS formulation for shell structures, eliminating locking via pressure projection. Casquero and Golestanian [53] proposed a NURBS-based continuous-assumed-strain element to alleviate volumetric locking. Most of these approximations offer better flexibility for arranging DOFs since their shape function constructions are no longer element-dependent. Huerta et al.[54] proposed a reproducing kernel approximation with divergence-free basis functions to avoid volumetric strain entirely , although this approach is unsuitable for compressible cases. Wu et al. [55] added extra displacement DOFs in FEM elements to resolve the locking issue, constructing local shape functions using generalized meshfree interpolation to maintain consistency. Vu-Huu et al. [56] employed different-order polygonal finite element shape functions to approximate displacement and pressure, embedding a bubble function in each element for stabilization.

This work proposes a more precise optimal volumetric constraint ratio and implements a locking-free mixed FE-meshfree formulation with this optimal constraint ratio. Firstly, the inf-sup condition is derived in a new form, showing that the inf-sup value equals to the lowest non-zero eigenvalue of dilatation stiffness in the context of variational analysis. Subsequently, involving a complete polynomial space with dimensions identical to displacement DOFs, the number of non-zero eigenvalues can be analytically calculated, and a new estimator considering the constraint ratio is established. From this estimator, the optimal constraint ratio is defined with a stabilized number of pressure nodes. If the constraint ratio exceeds the locking ratio, the formulation will show severe locking. When the constraint ratio is lower than the optimal ratio, the formulation achieves satisfactory results, and the inf-sup condition is fulfilled. This estimator provides a strong link between the inf-sup value and the pressure DOFs, making it possible to justify the locking status by counting the pressure nodes. Furthermore, a mixed FE-meshfree formulation is proposed to verify the optimal constraint ratio. In this mixed formulation, the displacement is approximated by traditional finite element methods, and the pressure is discretized by reproducing kernel meshfree approximation. With the aid of global RK shape functions, the pressure's DOFs can be adjusted arbitrarily without considering approximation order and numerical integration issues to maintaining the constraint ratio as optimal.

The remainder of this paper is organized as follows: Section 2 reviews the mixed formulation framework for incompressible elasticity problems. In Section 3, a novel estimator of the inf-sup value is developed, from which the optimal constraint ratio is obtained. Section 4 introduces the mixed FE-meshfree formulation and its corresponding nodal distribution schemes. Section 5 verifies the proposed optimal constraint ratio using a set of benchmark incompressible elasticity examples, studying error convergence and stability property for the mixed FE-meshfree approximation. Finally, the conclusions are presented in Section 6.

¹³⁶ **2. Mixed-formulation**

¹³⁷ *2.1. Nearly-incompressible elasticity*

¹³⁸ Consider a body $\Omega \in \mathbb{R}^{n_d}$ with boundary Γ in n_d -dimension, where Γ_t and
¹³⁹ Γ_g denote its natural boundary and essential boundary, respectively, such that
¹⁴⁰ $\Gamma_t \cup \Gamma_g = \Gamma$, $\Gamma_t \cap \Gamma_g = \emptyset$. The corresponding governing equations for the mixed
¹⁴¹ formulation are given by:

$$\begin{cases} \nabla \cdot \boldsymbol{\sigma} + \mathbf{b} = \mathbf{0} & \text{in } \Omega \\ \frac{p}{\kappa} + \nabla \cdot \mathbf{u} = 0 & \text{in } \Omega \\ \boldsymbol{\sigma} \cdot \mathbf{n} = \mathbf{t} & \text{on } \Gamma_t \\ \mathbf{u} = \mathbf{g} & \text{on } \Gamma_g \end{cases} \quad (2)$$

¹⁴² where \mathbf{b} denotes the prescribed body force in Ω . \mathbf{t}, \mathbf{g} are prescribed traction and
¹⁴³ displacement on natural and essential boundaries, respectively. \mathbf{u} and p , standing
¹⁴⁴ for displacement and hydrostatic pressure, respectively, are the variables of
¹⁴⁵ this problem. ∇ is the gradient tensor defined by $\nabla = \frac{\partial}{\partial x_i} \mathbf{e}_i$. $\boldsymbol{\sigma}$ denotes the
¹⁴⁶ stress tensor and has the following form:

$$\boldsymbol{\sigma}(\mathbf{u}, p) = p \mathbf{1} + 2\mu \nabla^d \mathbf{u} \quad (3)$$

¹⁴⁷ in which $\mathbf{1} = \delta_{ij} \mathbf{e}_i \otimes \mathbf{e}_j$ is the second-order identity tensor. $\nabla^d \mathbf{u}$ is the deviatoric
¹⁴⁸ gradient of \mathbf{u} and can be evaluated by:

$$\nabla^d \mathbf{u} = \frac{1}{2} (\mathbf{u} \nabla + \nabla \mathbf{u}) - \left(\frac{1}{3} \nabla \cdot \mathbf{u} \right) \mathbf{1} \quad (4)$$

¹⁴⁹ and κ, μ are the bulk modulus and shear modulus, respectively, and they can
¹⁵⁰ be represented by Young's modulus E and Poisson's ratio ν :

$$\kappa = \frac{E}{2(1-2\nu)}, \quad \mu = \frac{E}{3(1+\nu)} \quad (5)$$

¹⁵¹ In accordance with the Galerkin formulation, the weak form can be given
¹⁵² by: Find $\mathbf{u} \in V, p \in Q$, such that

$$\begin{cases} a(\mathbf{v}, \mathbf{u}) + b(\mathbf{v}, p) = f(\mathbf{v}) & \forall \mathbf{v} \in V \\ b(\mathbf{u}, q) + c(q, p) = 0 & \forall q \in Q \end{cases} \quad (6)$$

¹⁵³ with the spaces V, Q defined by:

$$V = \{\mathbf{v} \in H^1(\Omega)^2 \mid \mathbf{v} = \mathbf{g}, \text{ on } \Gamma_g\} \quad (7)$$

$$Q = \{q \in L^2(\Omega) \mid \int_{\Omega} q d\Omega = 0\} \quad (8)$$

¹⁵⁴ where $a : V \times V \rightarrow \mathbb{R}$, $b : V \times Q \rightarrow \mathbb{R}$ and $c : Q \times Q \rightarrow \mathbb{R}$ are bilinear forms,
¹⁵⁵ and $f : V \rightarrow \mathbb{R}$ is the linear form. In elasticity problems, they are given by:

$$a(\mathbf{v}, \mathbf{u}) = \int_{\Omega} \nabla^d \mathbf{v} : \nabla^d \mathbf{u} d\Omega \quad (9)$$

$$b(\mathbf{v}, q) = \int_{\Omega} \nabla \cdot \mathbf{v} q d\Omega \quad (10)$$

$$c(q, p) = - \int_{\Omega} \frac{1}{3\kappa} q p d\Omega \quad (11)$$

$$f(\mathbf{v}) = \int_{\Gamma_t} \mathbf{v} \cdot \mathbf{t} d\Gamma + \int_{\Omega} \mathbf{v} \cdot \mathbf{b} d\Omega \quad (12)$$

¹⁵⁶ *2.2. Ritz–Galerkin problem and volumetric locking*

¹⁵⁷ In the mixed-formulation framework, the displacement and pressure can be
¹⁵⁸ discretized by different approximations. The approximant displacement \mathbf{u}_h and
¹⁵⁹ approximant pressure p_h can be expressed by:

$$\mathbf{u}_h(\mathbf{x}) = \sum_{I=1}^{n_u} N_I(\mathbf{x}) \mathbf{u}_I, \quad p_h(\mathbf{x}) = \sum_{K=1}^{n_p} \Psi_K(\mathbf{x}) p_K \quad (13)$$

¹⁶⁰ where N_I and Ψ_K are the shape functions for the displacement and pressure, \mathbf{u}_I
¹⁶¹ and p_K are the corresponding coefficients. Leading these approximations into
¹⁶² the weak form of Eq. (6) yields the following Ritz–Galerkin problems: Find
¹⁶³ $\mathbf{u}_h \in V_h$, $p_h \in Q_h$, such that

$$\begin{cases} a(\mathbf{v}_h, \mathbf{u}_h) + b(\mathbf{v}_h, p_h) = f(\mathbf{v}_h) & \forall \mathbf{v}_h \in V_h \\ b(\mathbf{u}_h, q_h) + c(q_h, p_h) = 0 & \forall q_h \in Q_h \end{cases} \quad (14)$$

¹⁶⁴ where the spaces $V_h \subseteq V$, $Q_h \subseteq Q$ are defined by:

$$V_h = \{\mathbf{v}_h \in (\text{span}\{N_I\}_{I=1}^{n_u})^{n_d} | \mathbf{v}^h = \mathbf{g}, \text{ on } \Gamma_g\} \quad (15)$$

$$Q_h = \{q_h \in \text{span}\{\Psi_K\}_{K=1}^{n_p} | \int_{\Omega} q_h d\Omega = 0\} \quad (16)$$

¹⁶⁵ For nearly incompressible material, the Poisson ratio approaches 0.5, and
¹⁶⁶ the bulk modulus κ will tend to infinity based on Eq. (5). Then, the bilinear
¹⁶⁷ form c in Eq. (11) tends to zero. And the weak form of Eq. (14) becomes an
¹⁶⁸ enforcement of the volumetric strain $\nabla \cdot \mathbf{u}_h$ to be zero using the Lagrangian
¹⁶⁹ multiplier method, where p_h is the Lagrangian multiplier.

¹⁷⁰ Furthermore, from the second line of Eq. (14), we have:

$$b(\mathbf{u}_h, q_h) + c(q_h, p_h) = (q_h, \nabla \cdot \mathbf{u}_h) - (q_h, \frac{1}{3\kappa} p_h) = 0, \quad \forall q_h \in Q_h \quad (17)$$

¹⁷¹ or

$$(q_h, 3\kappa \nabla \cdot \mathbf{u}_h - p_h) = 0, \quad \forall q_h \in Q_h \quad (18)$$

¹⁷² where (\bullet, \bullet) is the inner product operator evaluated by:

$$(q, p) := \int_{\Omega} q p d\Omega \quad (19)$$

¹⁷³ Obviously, in Eq. (18), p_h is the orthogonal projection of $3\kappa \nabla \cdot \mathbf{u}_h$ with respect
¹⁷⁴ to the space Q_h [1], and, for further development, we use the nabla notation
¹⁷⁵ with an upper tilde to denote the projection operator, i.e., $p_h = \tilde{\nabla} \cdot \mathbf{u}_h$. In this
¹⁷⁶ circumstance, the bilinear form b in the first line of Eq. (14) becomes:

$$\begin{aligned} b(\mathbf{v}_h, p_h) &= (\underbrace{\nabla \cdot \mathbf{v}_h - \tilde{\nabla} \cdot \mathbf{v}_h, p_h}_{0}) + (\tilde{\nabla} \cdot \mathbf{v}_h, \underbrace{p_h}_{3\kappa \tilde{\nabla} \cdot \mathbf{u}_h}) \\ &= (\tilde{\nabla} \cdot \mathbf{v}_h, 3\kappa \tilde{\nabla} \cdot \mathbf{u}_h) \\ &= \tilde{a}(\mathbf{v}_h, \mathbf{u}_h) \end{aligned} \quad (20)$$

¹⁷⁷ where the bilinear form $\tilde{a} : V_h \times V_h \rightarrow \mathbb{R}$ is defined by:

$$\tilde{a}(\mathbf{v}_h, \mathbf{u}_h) = \int_{\Omega} 3\kappa \tilde{\nabla} \cdot \mathbf{v}_h \tilde{\nabla} \cdot \mathbf{u}_h d\Omega \quad (21)$$

¹⁷⁸ Accordingly, the problem of Eq. (14) becomes a one-variable form: Find
¹⁷⁹ $\mathbf{u}_h \in V_h$, such that

$$a(\mathbf{v}_h, \mathbf{u}_h) + \tilde{a}(\mathbf{v}_h, \mathbf{u}_h) = f(\mathbf{v}_h), \quad \forall \mathbf{v}_h \in V_h \quad (22)$$

¹⁸⁰ As $\kappa \rightarrow \infty$, Eq. (22) can be regarded as an enforcement of volumetric strain
¹⁸¹ using the penalty method, where \tilde{a} is the penalty term. However, it should
¹⁸² be noted that, if the mixed-formulation wants to obtain a satisfactory result,
¹⁸³ this orthogonal projection must be surjective [57]. In the case where it is not
¹⁸⁴ surjective, for a given $p_h \in Q_h$, it may not be possible to find a $\mathbf{u}_h \in V_h$ such that
¹⁸⁵ $p_h = 3\kappa \nabla \cdot \mathbf{u}_h$. This will lead to a much smaller displacement than expected and
¹⁸⁶ an oscillated pressure result. This phenomenon is called volumetric locking.

¹⁸⁷ 3. Optimal volumetric constraint ratio

¹⁸⁸ 3.1. Inf-sup condition and its eigenvalue problem

¹⁸⁹ To ensure the surjectivity of orthogonal projection and satisfactory results,
¹⁹⁰ the approximations of Eq.(7) should satisfy the inf-sup condition, also known
¹⁹¹ as the Ladyzhenskaya–Babuška–Brezzi condition [4]:

$$\inf_{q_h \in Q_h} \sup_{\mathbf{v}_h \in V_h} \frac{|b(q_h, \mathbf{v}_h)|}{\|q_h\|_Q \|\mathbf{v}_h\|_V} \geq \beta > 0 \quad (23)$$

¹⁹² in which β , namely the inf-sup value, is a constant independent of the charac-
¹⁹³ terized element size h . The norms $\|\bullet\|_V$ and $\|\bullet\|_Q$ can be flexibly defined

¹⁹⁴ by:

$$\|\mathbf{v}\|_V^2 := \int_{\Omega} \nabla^d \mathbf{v} : \nabla^d \mathbf{v} d\Omega \quad (24)$$

$$\|q\|_Q^2 := \int_{\Omega} \frac{1}{3\kappa} q^2 d\Omega \quad (25)$$

¹⁹⁵ To establish the relationship between the inf-sup condition and the constraint ratio, the inf-sup condition is firstly transformed by the following Lemma ¹⁹⁶ 1:

¹⁹⁸ **Lemma 1.** Suppose $\mathcal{P}_h : V_h \rightarrow Q_h$ is the orthogonal projection operator of the ¹⁹⁹ divergence operator $\mathcal{P} := 3\kappa \nabla \cdot$, i.e., $\mathcal{P}_h := 3\kappa \nabla \cdot$ and satisfies Eq. (18). Then, ²⁰⁰ the inf-sup value can be estimated by:

$$\beta \leq \inf_{V'_h \subset V_h \setminus \ker \mathcal{P}_h} \sup_{\mathbf{v}_h \in V'_h} \frac{\|\mathcal{P}_h \mathbf{v}_h\|_Q}{\|\mathbf{v}_h\|_V} \quad (26)$$

²⁰¹ in which $\ker \mathcal{P}_h \subset V_h$ is the kernel of \mathcal{P}_h defined by $\ker \mathcal{P}_h := \{\mathbf{v}_h \in V_h \mid \mathcal{P}_h \mathbf{v}_h = 0\}$.

²⁰³ PROOF. First, define the image space of \mathcal{P}_h as $\text{Im} \mathcal{P}_h := \{p_h \in Q_h \mid \exists \mathbf{v}_h \in V_h, p_h = \mathcal{P}_h \mathbf{v}_h\}$. Since $\mathcal{P}_h \subset Q_h$, Eq. (23) can be rewritten as:

$$\begin{aligned} \beta &\leq \inf_{q_h \in Q_h} \sup_{\mathbf{v}_h \in V_h} \frac{|b(q_h, \mathbf{v}_h)|}{\|q_h\|_Q \|\mathbf{v}_h\|_V} = \inf_{q_h \in Q_h} \sup_{\mathbf{v}_h \in V_h} \frac{|(q_h, \frac{1}{3\kappa} \mathcal{P} \mathbf{v}_h)|}{\|q_h\|_Q \|\mathbf{v}_h\|_V} \\ &\leq \inf_{q_h \in \text{Im} \mathcal{P}_h} \sup_{\mathbf{v}_h \in V_h} \frac{|\frac{1}{3\kappa} (q_h, \mathcal{P}_h \mathbf{v}_h)|}{\|q_h\|_Q \|\mathbf{v}_h\|_V} \end{aligned} \quad (27)$$

²⁰⁵ For a given $q_h \in \text{Im} \mathcal{P}_h$, since both q_h and $\mathcal{P}_h \mathbf{v}_h$ belong to $\text{Im} \mathcal{P}_h$, $\text{Im} \mathcal{P}_h \subset Q_h$, ²⁰⁶ according to the Cauchy-Schwarz inequality, we have:

$$\left| \frac{1}{3\kappa} (q_h, \mathcal{P}_h \mathbf{v}_h) \right| \leq \|q_h\|_Q \|\mathcal{P}_h \mathbf{v}_h\|_Q \quad (28)$$

²⁰⁷ where this equality holds if and only if $q_h = \mathcal{P}_h \mathbf{v}_h$, i.e.,

$$\left| \frac{1}{3\kappa} (q_h, \mathcal{P}_h \mathbf{v}_h) \right| = \|q_h\|_Q \|\mathcal{P}_h \mathbf{v}_h\|_Q, \quad \forall \mathbf{v}_h \in V'_h \quad (29)$$

²⁰⁸ the space $V'_h \subseteq V_h \setminus \ker \mathcal{P}_h$ defined by:

$$V'_h = \{\mathbf{v}_h \in V_h \mid \mathcal{P}_h \mathbf{v}_h = q_h\} \quad (30)$$

²⁰⁹ And the following relationship can be evidenced:

$$\sup_{\mathbf{v}_h \in V_h} \frac{|\frac{1}{3\kappa} (q_h, \mathcal{P}_h \mathbf{v}_h)|}{\|q_h\|_Q \|\mathbf{v}_h\|_V} = \sup_{\mathbf{v}_h \in V'_h} \frac{\|\mathcal{P}_h \mathbf{v}_h\|_Q}{\|\mathbf{v}_h\|_V}, \quad \exists q_h \in \text{Im} \mathcal{P}_h \quad (31)$$

²¹⁰ Consequently, by combining Eqs. (27) and (31), Eq. (26) can be obtained.

211 **Remark 1.** With Lemma 1 and the norm definitions in Eqs. (24),(25), the
212 square of the inf-sup value can further be bounded by:

$$\beta^2 \leq \inf_{V'_h \subset V_h \setminus \ker \mathcal{P}_h} \sup_{\mathbf{v}_h \in V'_h} \frac{\|\mathcal{P}_h \mathbf{v}_h\|_Q^2}{\|\mathbf{v}_h\|_V^2} = \inf_{V'_h \subset V_h \setminus \ker \mathcal{P}_h} \sup_{\mathbf{v}_h \in V'_h} \frac{\tilde{a}(\mathbf{v}_h, \mathbf{v}_h)}{a(\mathbf{v}_h, \mathbf{v}_h)} \quad (32)$$

213 The left-hand side of the above equation is consistent with the minimum-maximum
214 principle [58] and again proves the equivalence with the traditional numerical
215 inf-sup test [5]. Since that, β^2 evaluates the non-zero general eigenvalue of \tilde{a}
216 and a in Eq. (22).

217 3.2. Inf-sup value estimator

218 Subsequently, the relationship between constraint ratio and the inf-sup con-
219 dition is established by the following Theorem:

220 **Theorem 1.** Suppose that P_{n_u} is a complete polynomial space with n_u dimen-
221 sions, and V_{n_u} is the polynomial displacement space, $V_{n_u} = P_{n_u}^{n_d}$. The inf-sup
222 value β can further be bounded by:

$$\beta \leq \beta_s + O(h) \quad (33)$$

223 with

$$\beta_s = \inf_{V' \subset V_{n_u} \setminus \ker \mathcal{P}_h \mathcal{I}_h} \sup_{\mathbf{v} \in V'} \frac{\|\mathcal{P} \mathbf{v}\|_Q}{\|\mathbf{v}\|_V} \quad (34)$$

224 where \mathcal{I}_h is the interpolation operator of the displacement approximation, and
225 correspondingly, $O(h)$ is the remainder related to h .

226 PROOF. As the dimensions of V_h and V_{n_u} are identical, $\dim V_{n_u} = \dim V_h =$
227 $n_d \times n_u$. There exists a unique $\mathbf{v} \in V_{n_u}$ satisfying $\mathbf{v}_h = \mathcal{I}_h \mathbf{v}$. And the right side
228 of Eq. (26) becomes:

$$\inf_{V'_h \subset V_h \setminus \ker \mathcal{P}_h} \sup_{\mathbf{v}_h \in V'_h} \frac{\|\mathcal{P}_h \mathbf{v}_h\|_Q}{\|\mathbf{v}_h\|_V} = \inf_{V' \subset V_{n_u} \setminus \ker \mathcal{P}_h \mathcal{I}_h} \sup_{\mathbf{v} \in V'} \frac{\|\mathcal{P}_h \mathcal{I}_h \mathbf{v}\|_Q}{\|\mathcal{I}_h \mathbf{v}\|_V} \quad (35)$$

229 According to the triangular inequality, Cauchy-Schwarz inequality, and the
230 relationship of Eqs. (18), we have:

$$\begin{aligned} \|\mathcal{P}_h \mathcal{I}_h \mathbf{v}\|_Q &= \sup_{q_h \in Q_h} \frac{|\frac{1}{3\kappa}(q_h, \mathcal{P}_h \mathcal{I}_h \mathbf{v})|}{\|q_h\|_Q} = \sup_{q_h \in Q_h} \frac{|\frac{1}{3\kappa}(q_h, \mathcal{P} \mathcal{I}_h \mathbf{v})|}{\|q_h\|_Q} \\ &\leq \sup_{q_h \in Q_h} \frac{|\frac{1}{3\kappa}(q_h, \mathcal{P} \mathbf{v})| + |\frac{1}{3\kappa}(q_h, \mathcal{P} \mathbf{v} - \mathcal{P} \mathcal{I}_h \mathbf{v})|}{\|q_h\|_Q} \\ &\leq \|\mathcal{P} \mathbf{v}\|_Q + \|\mathcal{P}(\mathbf{v} - \mathcal{I}_h \mathbf{v})\|_Q \end{aligned} \quad (36)$$

231 Obviously, the second term on the right side of Eq. (36) is the interpolation
232 error, and can be evaluated by [59]:

$$\|\mathcal{P}(\mathbf{v} - \mathcal{I}_h \mathbf{v})\|_Q \leq Ch^k |\mathbf{v}|_{H_k} \quad (37)$$

233 where, for a sufficiently smooth $\mathbf{v} \in V$, k equals to the interpolation order of
 234 \mathcal{I}_h .

235 Further leading the relation $\|\mathcal{I}_h \mathbf{v}\|_V \geq C|\mathbf{v}|_{H_k}$ obtained from the closed
 236 graph theorem [33] and considering Eqs. (36)-(37), the right-hand side of Eq.
 237 (35) can be represented as:

$$\inf_{V' \subset V_{n_u} \setminus \ker \mathcal{P}_h \mathcal{I}_h} \sup_{\mathbf{v} \in V'} \frac{\|\mathcal{P}_h \mathcal{I}_h \mathbf{v}\|_Q}{\|\mathcal{I}_h \mathbf{v}\|_V} \leq \inf_{V' \subset V_{n_u} \setminus \ker \mathcal{P}_h \mathcal{I}_h} \sup_{\mathbf{v} \in V'} \frac{\|\mathcal{P} \mathbf{v}\|_Q}{\|\mathbf{v}\|_V} + O(h) \quad (38)$$

238 Substituting Eqs. (35),(38) into (26) finally proves Eqs. (33), (34).

239 As we can see in Eqs. (33) and (34), $\beta_s \geq 0$, the condition that β_s being
 240 equal to 0 or not determines whether the formulation can satisfy the inf-sup
 241 condition. If $\beta_s > 0$, as the mesh refines, the second term on the right-hand
 242 side of Eq. (33) will sharply reduce and can be ignored. In contrast, if $\beta_s = 0$,
 243 the second term will dominate, and the evaluation of β will be dependent to h .
 244 Therefore, the inf-sup condition is violated and numerical instability arises.

245 3.3. Polynomial-wise constraint counting

246 From the above subsection, we can know that whether β_s is zero or not
 247 determines whether the mixed-formulation can fulfill the inf-sup condition. Ac-
 248 cording to the expression of β_s in Eq. (34), as $\beta_s = 0$, the variable \mathbf{v} should
 249 belong to $\ker \mathcal{P}$, so the dimensions of the subspace in which $\beta_s \neq 0$, namely n_s ,
 250 can be evaluated by:

$$n_s = \dim(V_{n_u} \setminus \ker \mathcal{P}) \quad (39)$$

251 To further construct the relationship between the inf-sup value estimator in
 252 Eq. (33) and the constraint ratio $r = \frac{n_d \times n_u}{n_p}$, we should find the displacement
 253 and pressure DOFs in Eq. (33). With the definition of V_{n_u} , the number of
 254 displacement DOFs is easy to be evaluated by:

$$n_d \times n_u = \dim V_{n_u} \quad (40)$$

255 With well-posed nodal distributions of displacement and pressure, the number
 256 of pressure DOFs has the following relationship:

$$n_p = \dim Q_h = \dim(\text{Im} \mathcal{P}_h) = \dim(V_{n_u} \setminus \ker \mathcal{P}_h \mathcal{I}_h) \quad (41)$$

257 Figure 1 illustrates how the relationship between n_s , n_p , and n_u influences
 258 the fulfillment of the inf-sup condition:

- 259 • As $n_p > n_s$, there must exist a subspace in space $V_{n_u} \setminus \ker \mathcal{P}_h \mathcal{I}_h$ belonging
 260 to $\ker \mathcal{P}$, resulting in $\beta_s = 0$, i.e., $V_{n_u} \setminus \ker \mathcal{P}_h \mathcal{I}_h \cap \ker \mathcal{P} \neq \emptyset$. At this cir-
 261 cumstance, the inf-sup condition cannot be satisfied, and the formulation
 262 will suffer from volumetric locking.
- 263 • As $n_p \leq n_s$, for well-posed nodal distributions, the space $V_{n_u} \setminus \ker \mathcal{P}_h \mathcal{I}_h$
 264 may be a subset of $V_{n_u} \setminus \ker \mathcal{P}$. Then, β_s will remain nonzero, and the
 265 formulation will be locking-free.

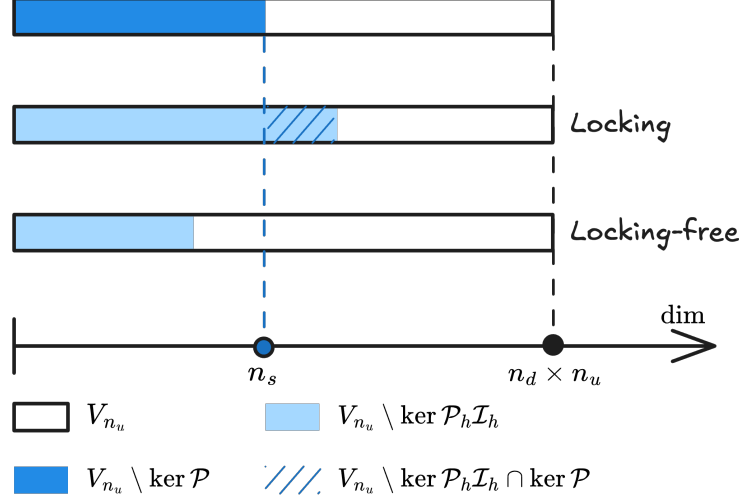


Figure 1: Illustration of estimator

266 Summarily, the formulation can satisfy the inf-sup condition and alleviate
 267 volumetric locking if at least the number of pressure nodes n_p is less than n_s ,
 268 so we name n_s as the stabilized number of pressure nodes. At this moment,
 269 the volumetric constraint ratio should meet the following relation to ensure the
 270 inf-sup condition:

$$r_{opt} \geq \frac{n_d \times n_u}{n_s} \quad (42)$$

271 **Remark 2.** *Some uniform elements with special arrangements, like the union-*
 272 *jack element arrangement for 3-node triangular elements, can pass the inf-sup*
 273 *test [6], but their pressure DOFs number is greater than n_s . This is because the*
 274 *union-jack arrangement leads to a lower nonzero eigenvalue number of $\tilde{\alpha}$ and a*
 275 *in Eq. (22), and the corresponding nonzero eigenvalue number is less than or*
 276 *equal to the stabilized number n_s , satisfying Eq. (42). The similar cases about*
 277 *this special element arrangement are too few, so it is more straightforward to*
 278 *use the number of pressure nodes n_p to measure $\dim(V_{n_u} \setminus \ker \mathcal{P}_h \mathcal{I}_h)$.*

279 **Remark 3.** *It is obvious that the traditional optimal constraint ratio cannot*
 280 *fulfill this condition. However, not all formulations satisfying this condition can*
 281 *totally avoid volumetric locking. This is because $n_p \leq n_s$ is not equivalent to*
 282 *$V_{n_u} \setminus \ker \mathcal{P}_h \mathcal{I}_h \subset V_{n_u} \setminus \ker \mathcal{P}$. Fortunately, well-posed nodal distributions of*
 283 *displacement and pressure can ensure this, which will be evidenced by numerical*
 284 *examples in the subsequent sections.*

285 3.4. Optimal volumetric constraint ratio

286 The fulfillment of the inf-sup condition should require the number of pres-
 287 sure nodes n_p to be lower than the stabilized number n_s , and now, we will
 288 demonstrate how to determine n_s for a specific number of displacement DOFs.

²⁸⁹ In the 2D case, for instance, we first consider the linear polynomial displace-
²⁹⁰ ment space V_3 that is given by:

$$V_3 = \text{span} \left\{ \begin{pmatrix} 1 \\ 0 \end{pmatrix}, \begin{pmatrix} 0 \\ 1 \end{pmatrix}, \begin{pmatrix} x \\ 0 \end{pmatrix}, \begin{pmatrix} 0 \\ x \end{pmatrix}, \begin{pmatrix} y \\ 0 \end{pmatrix}, \begin{pmatrix} 0 \\ y \end{pmatrix} \right\} \quad (43)$$

²⁹¹ or rearranged as follows,

$$V_3 = \text{span} \left\{ \underbrace{\begin{pmatrix} 1 \\ 0 \end{pmatrix}, \begin{pmatrix} 0 \\ 1 \end{pmatrix}, \begin{pmatrix} y \\ 0 \end{pmatrix}, \begin{pmatrix} 0 \\ x \end{pmatrix}, \begin{pmatrix} x \\ -y \end{pmatrix}}_{\ker \mathcal{P}}, \underbrace{\begin{pmatrix} x \\ y \end{pmatrix}}_{V_3 \setminus \ker \mathcal{P}} \right\} \quad (44)$$

²⁹² It can be counted that, for $n_u = 3$, $n_s = 1$. Following the path, the displacement
²⁹³ space with a quadratic polynomial base, namely V_6 , can be stated as:

$$V_6 = \text{span} \left\{ \underbrace{\begin{pmatrix} 1 \\ 0 \end{pmatrix}, \begin{pmatrix} 0 \\ 1 \end{pmatrix}, \begin{pmatrix} y \\ 0 \end{pmatrix}, \begin{pmatrix} 0 \\ x \end{pmatrix}, \begin{pmatrix} x \\ -y \end{pmatrix}, \begin{pmatrix} x^2 \\ -2xy \end{pmatrix}, \begin{pmatrix} y^2 \\ 0 \end{pmatrix}, \begin{pmatrix} 0 \\ x^2 \end{pmatrix}, \begin{pmatrix} -2xy \\ y^2 \end{pmatrix}}_{\ker \mathcal{P}}, \underbrace{\begin{pmatrix} x \\ y \end{pmatrix}, \begin{pmatrix} x^2 \\ 2xy \end{pmatrix}, \begin{pmatrix} 2xy \\ y^2 \end{pmatrix}}_{V_6 \setminus \ker \mathcal{P}} \right\} \quad (45)$$

²⁹⁴ In this circumstance, $n_s = 3$. As the order of the polynomial space increases,
²⁹⁵ the optimal numbers of constraint DOFs for each order of the polynomial space
²⁹⁶ are listed in Table. 1, in which n denotes the order of space P_{n_u} . For the
²⁹⁷ flexibility of usage, the relation between n_u and n_s is summarized as follows:

$$n_s = \frac{n(n+1)}{2}, \quad n = \left\lfloor \frac{\sqrt{1+8n_u}-3}{2} \right\rfloor \quad (46)$$

²⁹⁸ where $\lfloor \bullet \rfloor$ denotes the floor function.

Table 1: Relationship between the number of displacement nodes n_u and stabilized number of pressure nodes n_s

n	2D		3D	
	n_u	n_s	n_u	n_s
1	3	1	4	1
2	6	3	10	4
3	10	6	20	10
4	15	10	35	20
\vdots	\vdots	\vdots	\vdots	\vdots

²⁹⁹ For the 3D case, following the path in 2D, the linear polynomial space V_4 is

³⁰⁰ considered herein, and the arranged space of V_4 is listed as follows:

$$V_4 = \text{span} \left\{ \begin{array}{c} \underbrace{\left(\begin{array}{c} 1 \\ 0 \\ 0 \end{array} \right), \left(\begin{array}{c} 0 \\ 1 \\ 0 \end{array} \right), \left(\begin{array}{c} 0 \\ 0 \\ 1 \end{array} \right)}_{\ker \mathcal{P}}, \underbrace{\left(\begin{array}{c} 0 \\ x \\ 0 \end{array} \right), \left(\begin{array}{c} 0 \\ 0 \\ x \end{array} \right), \left(\begin{array}{c} 0 \\ 0 \\ 0 \end{array} \right)}_{\ker \mathcal{P}}, \left(\begin{array}{c} y \\ 0 \\ 0 \end{array} \right), \\ \underbrace{\left(\begin{array}{c} 0 \\ y \\ 0 \end{array} \right), \left(\begin{array}{c} z \\ 0 \\ 0 \end{array} \right), \left(\begin{array}{c} 0 \\ z \\ 0 \end{array} \right)}_{\ker \mathcal{P}}, \underbrace{\left(\begin{array}{c} x \\ -y \\ 0 \end{array} \right), \left(\begin{array}{c} x \\ 0 \\ -z \end{array} \right), \left(\begin{array}{c} x \\ y \\ z \end{array} \right)}_{V_{n_u} \setminus \ker \mathcal{P}} \end{array} \right\} \quad (47)$$

³⁰¹ For brevity, the stabilized numbers for higher-order polynomial displacement
³⁰² spaces are directly listed in Table. 1, and it can be summarized that, for a given
³⁰³ number of displacement DOFs, the stabilized number for pressure DOFs can be
³⁰⁴ calculated as follows:

$$n_s = \frac{n(n+1)(n+2)}{6} \quad (48)$$

$$n = \left[\left(3n_u + \frac{1}{3} \sqrt{81n_u^2 - \frac{1}{3}} \right)^{\frac{1}{3}} + \frac{1}{3 \left(3n_u + \frac{1}{3} \sqrt{81n_u^2 - \frac{1}{3}} \right)^{\frac{1}{3}}} - 2 \right] \quad (49)$$

³⁰⁵ 4. Mixed FE–meshfree formulation with optimal constraint ratio

³⁰⁶ In the proposed mixed–formulation, the displacement is approximated using
³⁰⁷ 3-node (Tri3), 6-node (Tri6) triangular elements and 4-node (Quad4), 8-node
³⁰⁸ (Quad8) quadrilateral elements in 2D, 4-node (Tet4) tetrahedral element and
³⁰⁹ 8-node (Hex8) hexahedral element in 3D [2]. In order to flexibly adjust to
³¹⁰ let the DOFs of pressure meet the optimal constraint, the reproducing kernel
³¹¹ meshfree approximation is involved to approximate pressure.

³¹² 4.1. Reproducing kernel meshfree approximation

³¹³ In accordance with the reproducing kernel approximation, the entire domain
³¹⁴ Ω , as shown in Figure 2, is discretized by n_p meshfree nodes, $\{\mathbf{x}_I\}_{I=1}^{n_p}$. The
³¹⁵ approximated pressure, namely p_h , can be expressed by the shape function Ψ_I
³¹⁶ and nodal coefficient p_I , yields:

$$p_h(\mathbf{x}) = \sum_{I=1}^{n_p} \Psi_I(\mathbf{x}) p_I \quad (50)$$

³¹⁷ where, in the reproducing kernel approximation framework, the shape function
³¹⁸ Ψ_I is given by:

$$\Psi_I(\mathbf{x}) = \mathbf{c}(\mathbf{x}_I - \mathbf{x}) \mathbf{p}(\mathbf{x}_I - \mathbf{x}) \phi(\mathbf{x}_I - \mathbf{x}) \quad (51)$$

³¹⁹ in which \mathbf{p} is the basis vector, for instance in the context of the 3D quadratic
³²⁰ case, the basis vector takes the following form:

$$\mathbf{p}(\mathbf{x}) = \{1, x, y, z, x^2, y^2, z^2, xy, xz, yz\}^T \quad (52)$$

³²¹ and ϕ stands for the kernel function. In this work, the traditional Cubic B-spline
³²² function with square or cube support is used as the kernel function:

$$\phi(\mathbf{x}_I - \mathbf{x}) = \phi(s_x)\phi(s_y)\phi(s_z), \quad s_i = \frac{\|\mathbf{x}_I - \mathbf{x}\|}{\bar{s}_{iI}} \quad (53)$$

³²³ with

$$\phi(s) = \frac{1}{3!} \begin{cases} (2-2s)^3 - 4(1-2s)^3 & s \leq \frac{1}{2} \\ (2-2s)^3 & \frac{1}{2} < s < 1 \\ 0 & s > 1 \end{cases} \quad (54)$$

³²⁴ where \bar{s}_{iI} 's are the support size towards the i -direction for the shape function
³²⁵ Ψ_I . The correction function \mathbf{c} can be determined by the following so-called
³²⁶ consistency condition:

$$\sum_{I=1}^{n_p} \Psi_I(\mathbf{x}) \mathbf{p}(\mathbf{x}_I) = \mathbf{p}(\mathbf{x}) \quad (55)$$

³²⁷ or equivalent shifted form:

$$\sum_{I=1}^{n_p} \Psi_I(\mathbf{x}) \mathbf{p}(\mathbf{x}_I - \mathbf{x}) = \mathbf{p}(\mathbf{0}) \quad (56)$$

³²⁸ The consistency condition ensures that the reproducing kernel shape functions
³²⁹ are able to reproduce the polynomial space spanned by the basis function \mathbf{p} ,
³³⁰ which is a fundamental requirement for the accuracy of the Galerkin method.
³³¹ Herein, the order of the basis function \mathbf{p} is chosen to be the same as the order
³³² of the displacement approximation.

³³³ Further, substituting Eq. 51 into Eq. (56) leads to:

$$\mathbf{c}(\mathbf{x}_I - \mathbf{x}) = \mathbf{A}^{-1}(\mathbf{x}_I - \mathbf{x}) \mathbf{p}(\mathbf{0}) \quad (57)$$

³³⁴ in which \mathbf{A} is namely the moment matrix evaluated by:

$$\mathbf{A}(\mathbf{x}_I - \mathbf{x}) = \sum_{I=1}^{n_p} \mathbf{p}(\mathbf{x}_I - \mathbf{x}) \mathbf{p}^T(\mathbf{x}_I - \mathbf{x}) \phi(\mathbf{x}_I - \mathbf{x}) \quad (58)$$

³³⁵ Taking Eq. (57) back to Eq. (51), the final form of the reproducing kernel shape
³³⁶ function can be obtained as:

$$\Psi_I(\mathbf{x}) = \mathbf{p}^T(\mathbf{0}) \mathbf{A}^{-1}(\mathbf{x}_I - \mathbf{x}) \phi(\mathbf{x}_I - \mathbf{x}) \quad (59)$$

³³⁷ As shown in Figure 2, reproducing kernel meshfree shape functions are glob-
³³⁸ ally smooth across the entire domain, using them to discretize the pressure field

339 allows the constraint ratio to be adjusted arbitrarily, without being limited by
 340 element topology. Meshfree shape functions generally lack the Kronecker delta
 341 property, which prevents the direct imposition of essential boundary conditions.
 342 Fortunately, the mixed formulation shown in Eq. 14 only concerns the displace-
 343 ment essential boundary condition, and this condition can be easily imposed by
 344 the standard methods, such as the penalty method that used in this work.

345 Moreover, when combined with finite element approximations in Eq. 14,
 346 numerical integration can be conveniently performed within each finite element
 347 (Ω_C 's). The numerical integration issue caused by the loss of variational con-
 348 sistency between meshfree shape functions and their derivatives [60] would not
 349 appear in the mixed formulation of Eq. 14, this is due to the fact that Eq.
 350 14 solely depends on the meshfree shape functions themselves. Therefore, the
 351 proposed method employs standard lower-order Gaussian quadrature rules, as
 352 commonly used in traditional finite element methods, while still maintaining its
 353 accuracy.

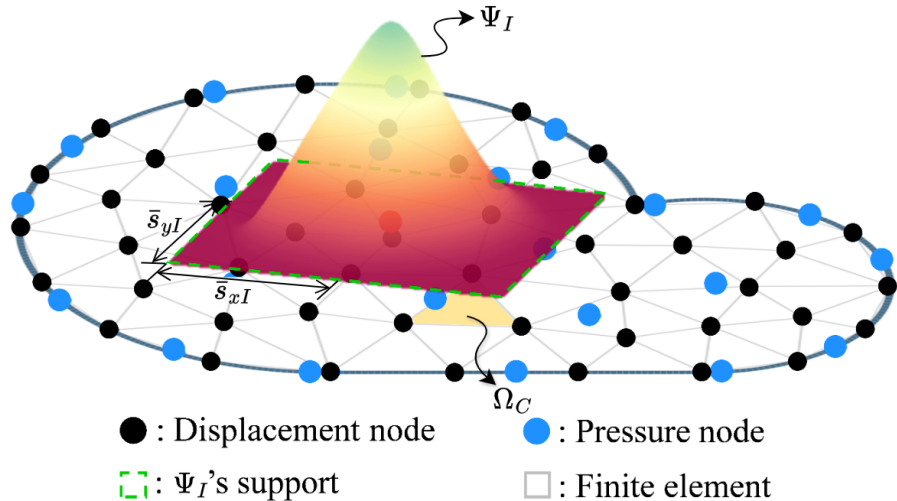


Figure 2: Illustration for reproducing kernel meshfree approximation

354 4.2. Pressure node distributions with optimal constraint ratio

355 In this subsection, 2D and 3D inf-sup tests [6], as defined in Eq. 32, are
 356 conducted using the mixed FE-meshfree formulations to validate the proposed
 357 inf-sup value estimator. The 2D test considers the square domain $\Omega = (0, 1) \times$
 358 $(0, 1)$, where the displacement is discretized by Tri3 and Quad4 with 4×4 ,
 359 8×8 , 16×16 and 32×32 elements, Tri6 and Quad8 with 2×2 , 4×4 , 8×8
 360 and 16×16 elements, respectively. The 3D test employs a cube domain $\Omega =$
 361 $(0, 1) \times (0, 1) \times (0, 1)$ with 4×4 , 8×8 and 16×16 elements for the Tet4 and Hex8.
 362 For pressure discretization, linear meshfree approximation with a normalized
 363 support size of 1.5 is employed for Tri3, Quad4, Tet4 and Hex8. For Tri6 and

364 Quad8, a quadratic meshfree approximation with a normalized support size of
 365 2.5 is utilized. In order to avoid the influence of interpolation error, uniform
 366 nodal distributions are used for pressure discretizations, for example in Figure
 367 3, which displays 4×4 Quad4 elements with 4×3 uniformly distributed pressure
 368 nodes.

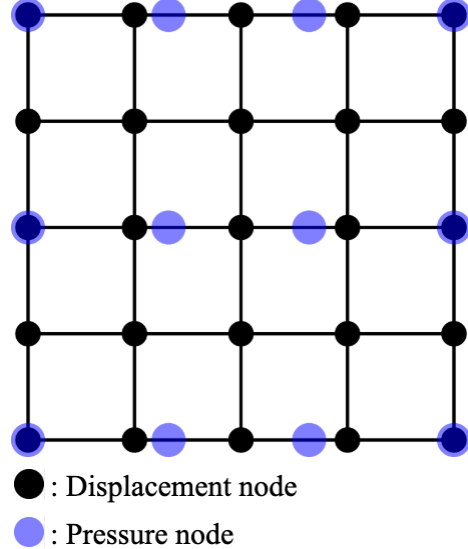


Figure 3: Illustration of uniform nodal distribution for inf-sup test with $n_u = 5 \times 5$, $n_p = 4 \times 3$

369 Figures 4–9 show the corresponding results, in which the red line stands for
 370 the value of β with respect to the number of pressure nodes n_p , and the vertical
 371 dashed line denotes the stabilized number n_s . The deeper color of the lines
 372 means mesh refinement. The results show that, no matter linear or quadratic
 373 elements, as n_p increases over n_s , the value of β sharply decreases, and then
 374 the inf-sup condition cannot be maintained. This result is consistent with the
 375 discussion in Section 3, and again verifies the effect of the proposed estimator.

376 Moreover, the mixed formulation's results with the traditional optimal con-
 377 straint ratio $r = n_d$ are listed in these figures as well, and β in this circumstance
 378 is already much smaller than those in the optimal range. Considering the re-
 379 sults shown above, the easy programming and efficiency, the pressure nodes
 380 are chosen among the displacement nodes. The optimal schemes for linear and
 381 quadratic, 2D and 3D element discretizations, namely with $r = r_{opt}$, are shown
 382 in Figure 10, where every other displacement node is selected as the pressure
 383 node. For practical implementations of linear cases, the pressure nodes are ini-
 384 tially generated using traditional approaches, such as Delaunay triangulation.
 385 Subsequently, the displacement nodes are then obtained through a standard
 386 mesh refinement process to the pressure nodes. For quadratic approximations
 387 in Tri6 and Quad8 elements, the element vertices are chosen as pressure nodes

388 after displacement element generation. Consequently, all constraint ratios evaluated
 389 using the discretizations in Figure 10 fall within the optimal range. The
 390 corresponding inf-sup test results for these schemes are also marked in inf-sup
 391 test figure and show that, with mesh refinement, their β 's are always maintained
 392 at a non-negligible level.

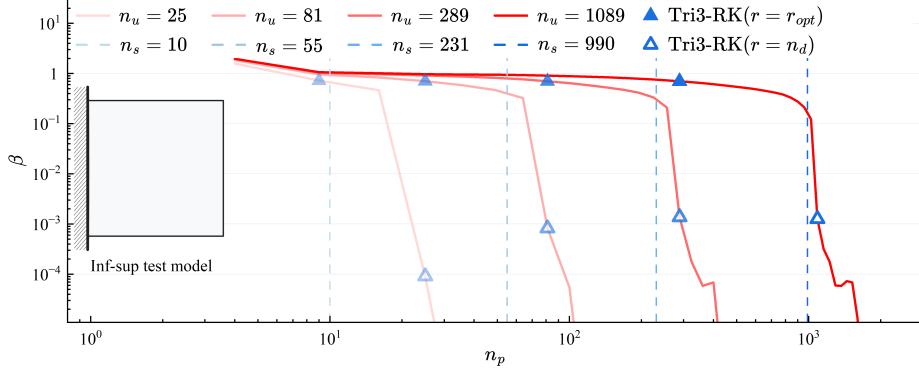


Figure 4: Inf-sup test for Tri3-RK

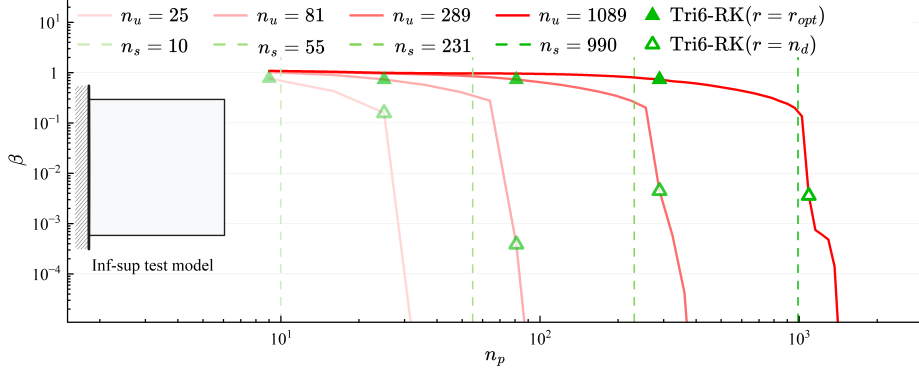


Figure 5: Inf-sup test for Tri6-RK

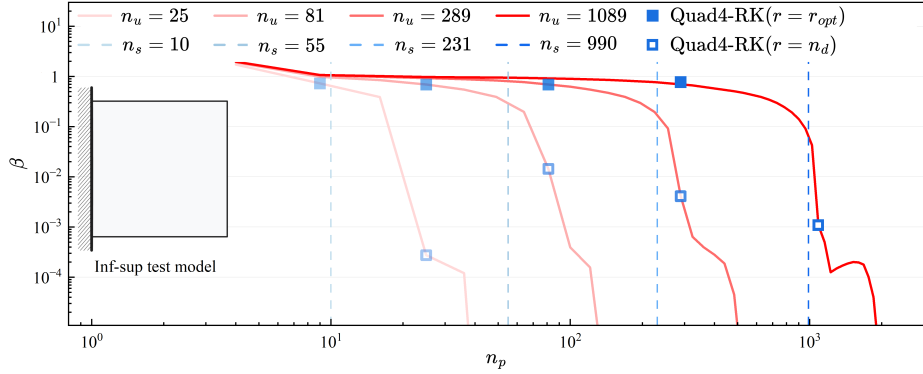


Figure 6: Inf-sup test for Quad4-RK

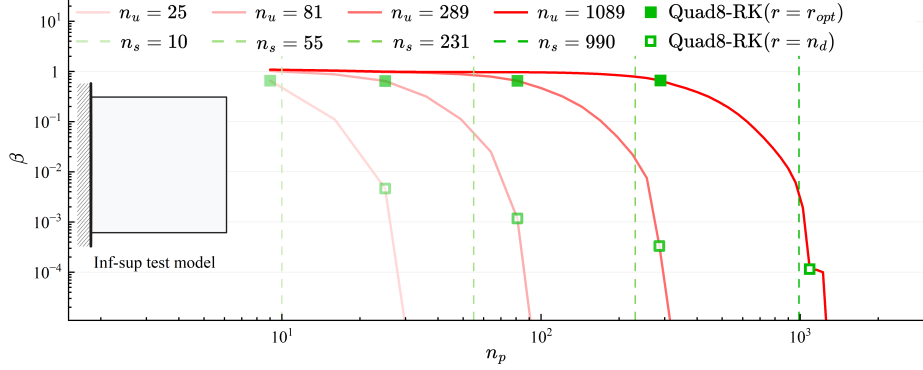


Figure 7: Inf-sup test for Quad8-RK

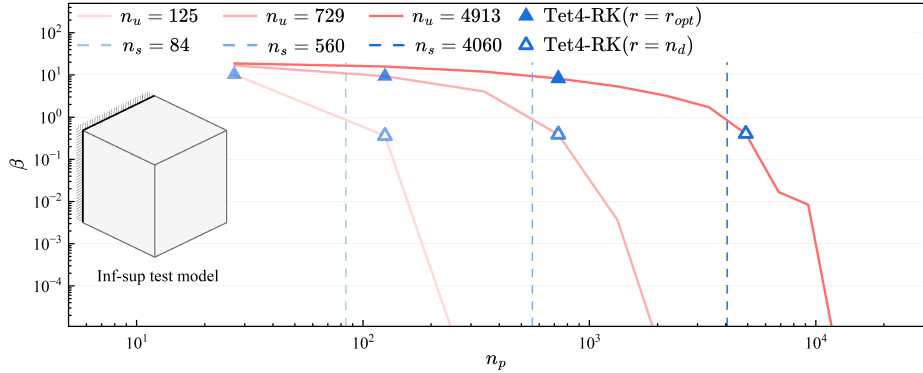


Figure 8: Inf-sup test for Tet4-RK

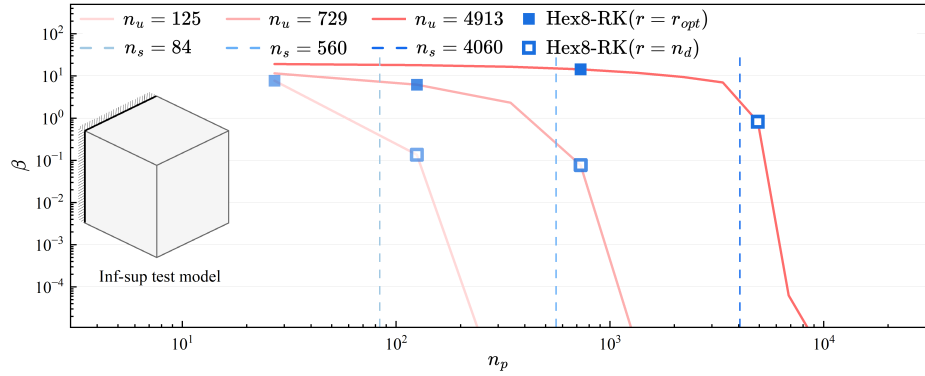


Figure 9: Inf-sup test for Hex8-RK

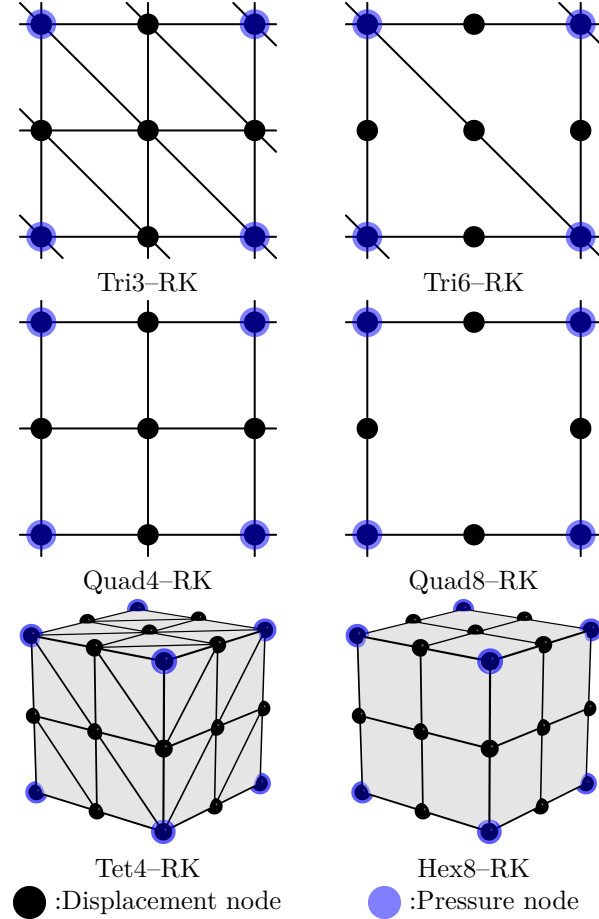


Figure 10: Nodal distribution schemes for mixed FE-meshfree formulations with $r = r_{opt}$

393 **5. Numerical examples**

394 *5.1. Cantilever beam problem*

395 Consider the cantilever beam problem shown in Figure 11 with length $L =$
 396 48, width $D = 12$, and the incompressible material parameters are employed
 397 with Young's modulus $E = 3 \times 10^6$, Poisson's ratio $\nu = 0.5 - 10^{-8}$. The left hand
 398 side is fixed and the right side subject to a concentrated force $P = 1000$. All
 399 the prescribed values in the boundary conditions are evaluated by the analytical
 400 solution that is given as follows [61]:

$$\begin{cases} u_x(x) = -\frac{Py}{6\bar{E}I} \left((6L - 3x)x + (2 + \bar{\nu})(y^2 - \frac{D^2}{4}) \right) \\ u_y(x) = \frac{P}{6\bar{E}I} \left(3\bar{\nu}y^2(L - x) + (4 + 5\bar{\nu})\frac{D^2x}{4} + (3L - x)x^2 \right) \end{cases} \quad (60)$$

401 where I is the beam's moment of inertia, \bar{E} and $\bar{\nu}$ are the material parameters
 402 for plane strain hypothesis, they can be expressed by:

$$I = \frac{D^3}{12}, \quad \bar{E} = \frac{E}{1 - \nu^2}, \quad \bar{\nu} = \frac{\nu}{1 - \nu} \quad (61)$$

403 And correspondingly, the stress components are evaluated by

$$\begin{cases} \sigma_{xx} = -\frac{P(L - x)y}{I} \\ \sigma_{yy} = 0 \\ \sigma_{xy} = \frac{P}{2I} \left(\frac{D^2}{4} - y^2 \right) \end{cases} \quad (62)$$

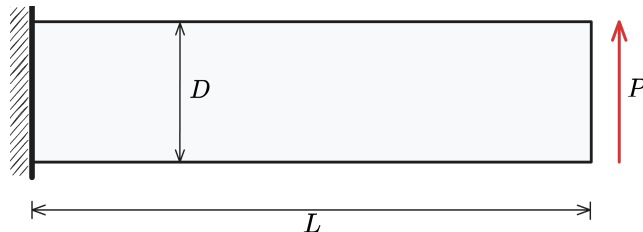


Figure 11: Illustration of cantilever beam problem

404 In this problem, the Quad4 element with 16×4 , 32×8 , 64×16 , 128×32
 405 grids, and Quad8 element with 8×2 , 16×4 , 32×8 , 64×16 grids are em-
 406 ployed for displacement discretization. The pressure is discretized by linear and
 407 quadratic meshfree approximations with 1.5 and 2.5 characterized support sizes
 408 respectively. The strain and pressure errors with respect to pressure nodes n_p
 409 are displayed in Figure 12, where, to avoid the interpolation error, the pres-
 410 sure nodes are uniformly distributed independent with displacement nodes by

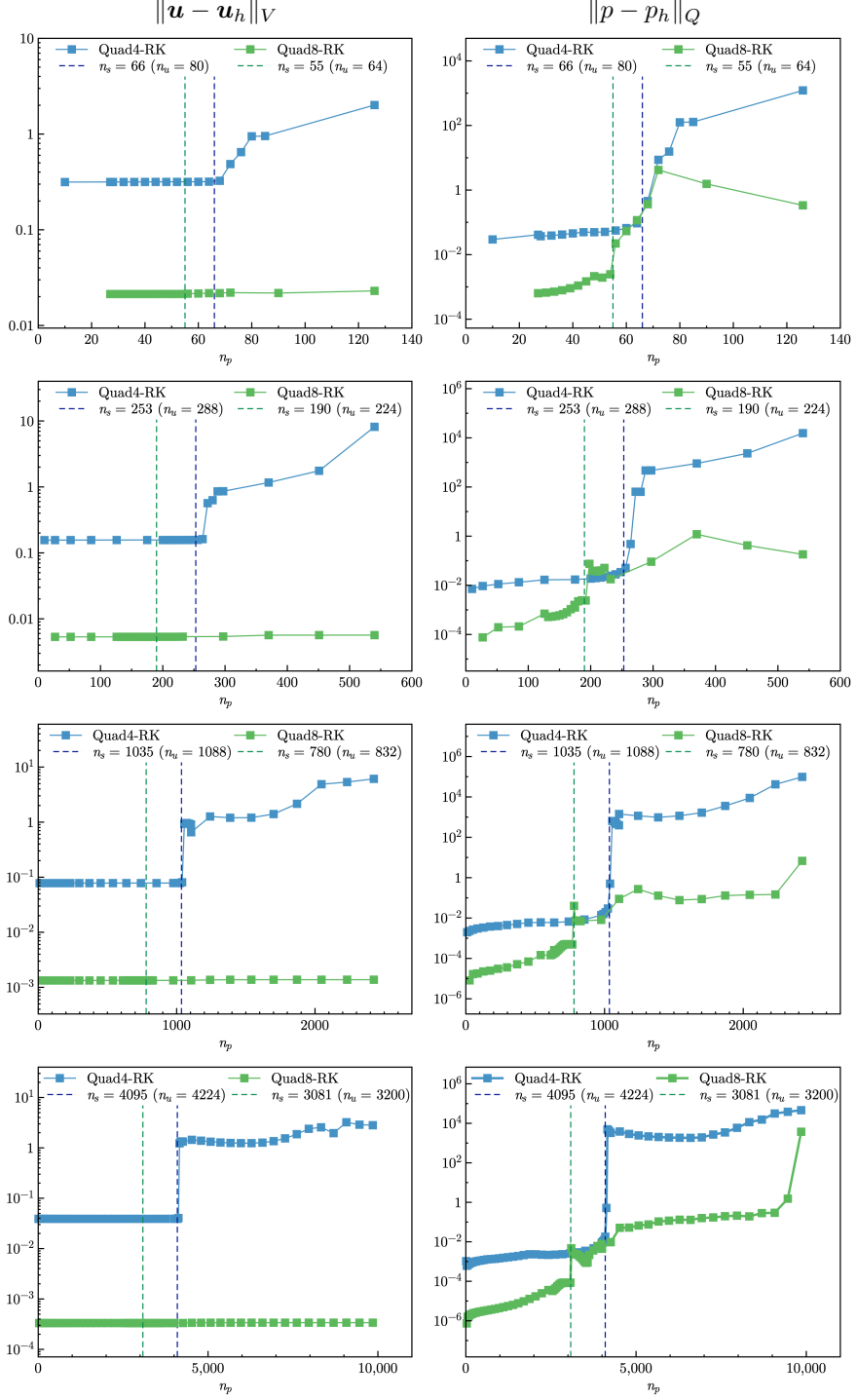


Figure 12: Strain and pressure errors vs. n_p for cantilever beam problem

the same way in Section 4.2. The vertical dashed lines stand for the stabilized number n_s . The figure implies that the Quad8 shows better performance than Quad4, since the Quad8's strain results are stable no matter the constraint ratio is in the optimal range or not. And the Quad4's displacement errors increase as soon as $n_p > n_s$. However, both Quad4's and Quad8's pressure errors immediately increase while their constraint ratios are out of the optimal range, and Quad8 still has better results than Quad4. Figure 13 shows the strain and pressure error convergence comparisons with Quad4-RK, Quad8-RK with $r = n_d$, $r = r_{opt}$ and traditional 4-node quadrilateral displacement element with 1-node piecewise constant pressure (Q4P1), 8-node quadrilateral displacement element with 3-node piecewise linear pressure (Q8P3) for this cantilever beam problem, in which, except Quad8-RK($r = n_d$) for strain error, all formulations with the traditional constraint ratio of $r = n_d$ cannot ensure the optimal error convergence rates. The proposed mixed formulations with $r = r_{opt}$ and Q4P1, Q8P3 can maintain the optimal error convergence ratio, except the strain error of Quad8-RK is a little larger than that of Q8P3, the proposed approaches show the best performance in accuracy.

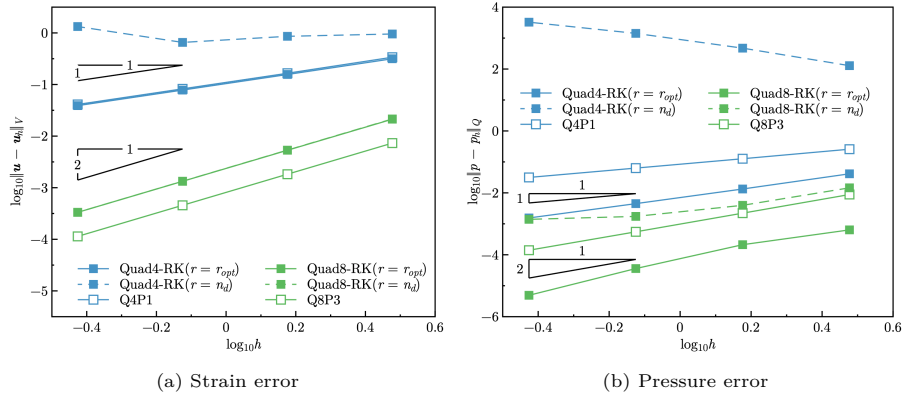


Figure 13: Error convergence study for cantilever beam problem

5.2. Plate with hole problem

Consider an infinite plate with a hole centered at the origin, as shown in Figure 14, and at the infinity towards the x -direction subjected to a uniform traction $T = 1000$. The geometric and material parameters for this problem are that the ratio of the hole $a = 1$, Young's modulus $E = 3 \times 10^6$, and Poisson's ratio $\nu = 0.5 - 10^{-8}$. The analytical solution of this problem refers to the Michell solution [61] as:

$$\begin{cases} u_x(\rho, \theta) = \frac{Ta}{8\mu} \left(\frac{\rho}{a}(k+1) \cos \theta - \frac{2a^3}{\rho^3} \cos 3\theta + \frac{2a}{\rho} ((1+k) \cos \theta + \cos 3\theta) \right) \\ u_y(\rho, \theta) = \frac{Ta}{8\mu} \left(\frac{\rho}{a}(k-3) \sin \theta - \frac{2a^3}{\rho^3} \sin 3\theta + \frac{2a}{\rho} ((1-k) \sin \theta + \sin 3\theta) \right) \end{cases} \quad (63)$$

435 in which $k = \frac{3-\nu}{1+\nu}$, $\mu = \frac{E}{2(1+\nu)}$. And the stress components are given by:

$$\begin{cases} \sigma_{xx} = T \left(1 - \frac{a^2}{\rho^2} \left(\frac{3}{2} \cos 2\theta + \cos 4\theta \right) + \frac{3a^4}{2\rho^4} \cos 4\theta \right) \\ \sigma_{yy} = -T \left(\frac{a^2}{\rho^2} \left(\frac{1}{2} \cos 2\theta - \cos 4\theta \right) + \frac{3a^4}{2\rho^4} \cos 4\theta \right) \\ \sigma_{xy} = -T \left(\frac{a^2}{\rho^2} \left(\frac{1}{2} \sin 2\theta + \sin 4\theta \right) - \frac{3a^4}{2\rho^4} \sin 4\theta \right) \end{cases} \quad (64)$$

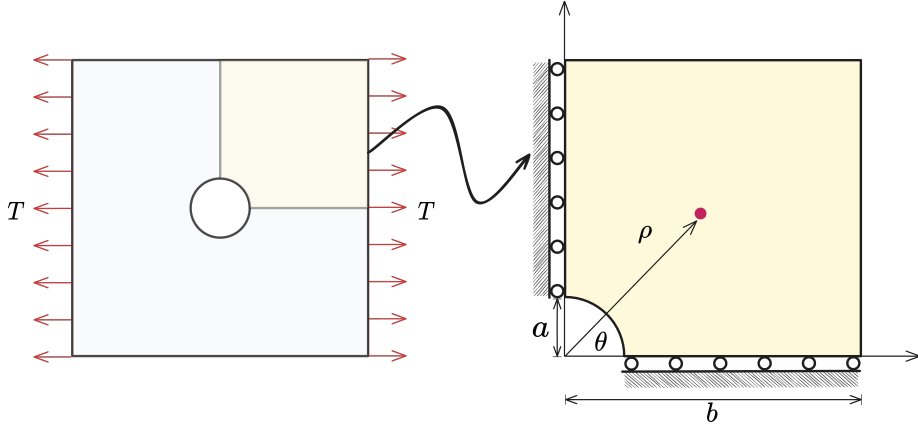


Figure 14: Illustration of plate with hole problem

436 According to the symmetry property of this problem, only a quarter model
 437 with length $b = 5$ is considered as shown in Figure 14. The displacement is
 438 discretized by 3-node and 6-node triangular elements with 81, 299, 1089, and
 439 4225 nodes. The corresponding linear and quadratic meshfree formulations are
 440 employed for pressure discretization, and the characterized support sizes are
 441 chosen as 1.5 and 2.5, respectively. Figure 15 studies the relationship between
 442 strain, pressure errors, and n_p using the nodal distributions uniformly related
 443 to displacement nodes. Unlike the quadrilateral element case in Section 5.1,
 444 the quadratic Tri6-RK shows worse results while the constraint ratio is out of
 445 the optimal range. And Tri3-RK exhibits less sensitivity in strain error than
 446 Tri6-RK, but its error is increasing while n_p goes up. Both Tri3-RK and Tri6-
 447 RK with constraint ratios under the optimal range perform acceptably. The
 448 corresponding error convergence study is presented in Figure 16, the traditional
 449 MINI element and the 6-node triangular displacement element with 3-node
 450 continuous triangular pressure element (T6C3) are employed for comparison.
 451 The results show that only Tri3-RK with $r = 2$ shows a comparable result with
 452 the optimal one with $r = r_{opt}$. The other formulations with the traditional
 453 constraint ratio show lower accuracy and error convergence rates.

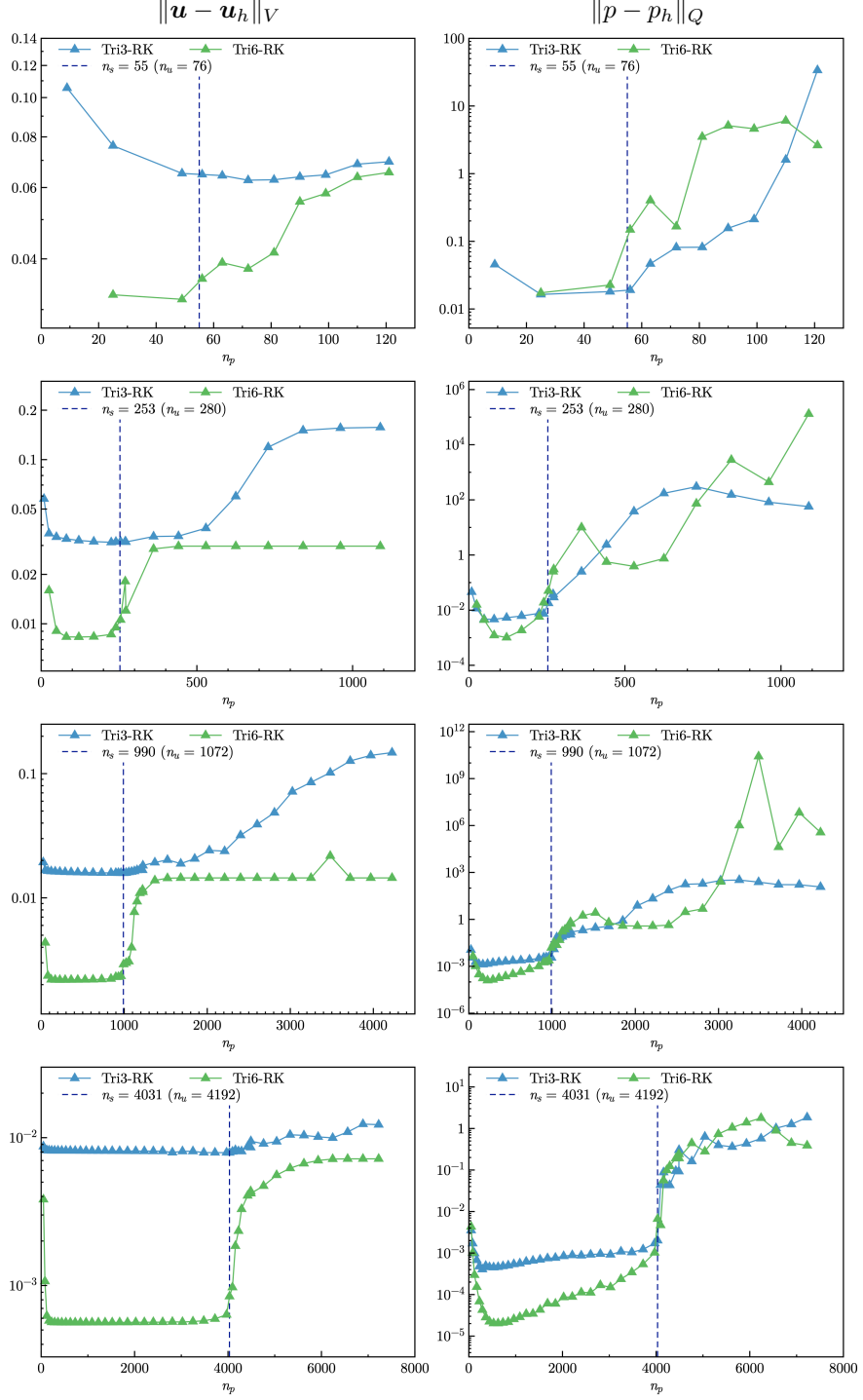


Figure 15: Strain and pressure errors vs. n_p for plate with hole problem

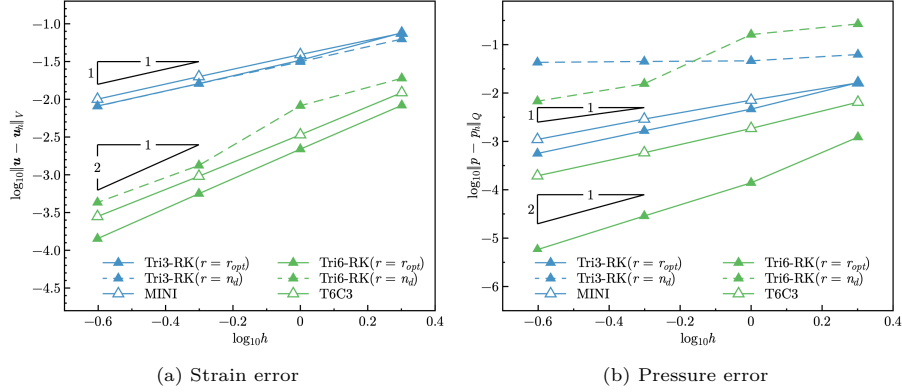


Figure 16: Error convergence study for plate with a hole problem

454 5.3. Cook's membrane problem

455 The Cook's membrane problem [12] is used herein for stability analysis of
 456 pressure. The geometry of this problem is shown in Figure 17, in which the left
 457 hand side is fixed and the right hand side subjects a concentrated force $P = 6.25$
 458 in the y -direction. The material parameters are Young's modulus $E = 70.0$ and
 459 Poisson's ratio $\nu = 0.5 - 10^{-8}$.

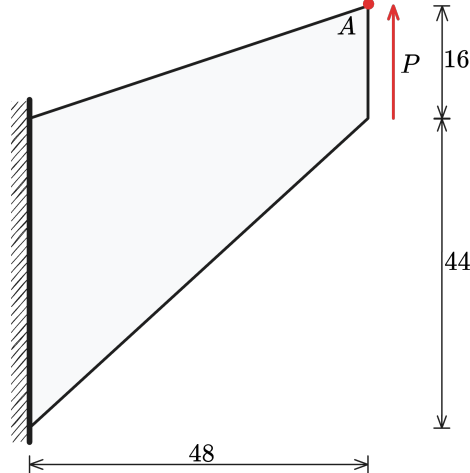


Figure 17: Illustration of Cook's membrane problem

460 In this test, we evaluated the convergence properties by comparing the ver-
 461 tical displacement at point A against a reference value of 28.0. As shown in
 462 Figure 18 illustrates, the methods employing $r = r_{opt}$ produced results that
 463 were notably closer to this reference value than those using $r = n_d$. Further-
 464 more, to investigate stability, Figures 19–22 show the pressure contour plots for
 465 non-uniform Tri3–RK, Tri6–RK, Quad4–RK, and Quad8–RK formulations with

466 $r = n_d$ and $r = r_{opt}$, respectively. The reproducing kernel meshfree approxima-
 467 tions are employed for pressure discretization with characterized support sizes
 468 of 1.5 for the linear basis function and 2.5 for the quadratic basis function. The
 469 results imply that the pressure contour plots with the optimal constraint ratio
 470 $r = r_{opt}$ show a more stable and smooth pressure distribution compared to those
 471 with the traditional constraint ratio $r = n_d$.

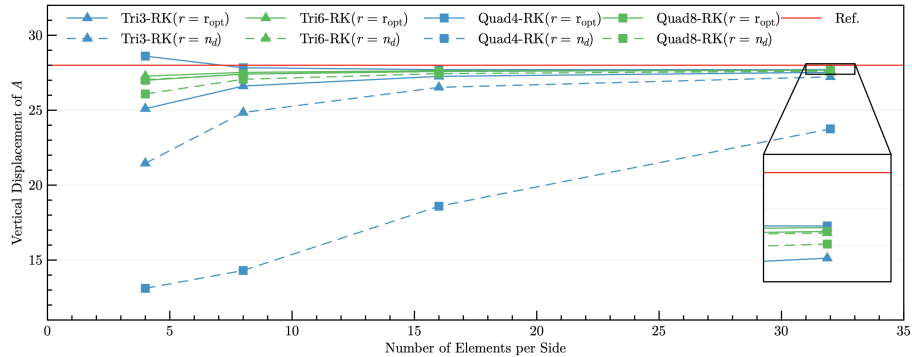


Figure 18: Convergence comparison of the vertical displacement at point A for Cook's membrane problem

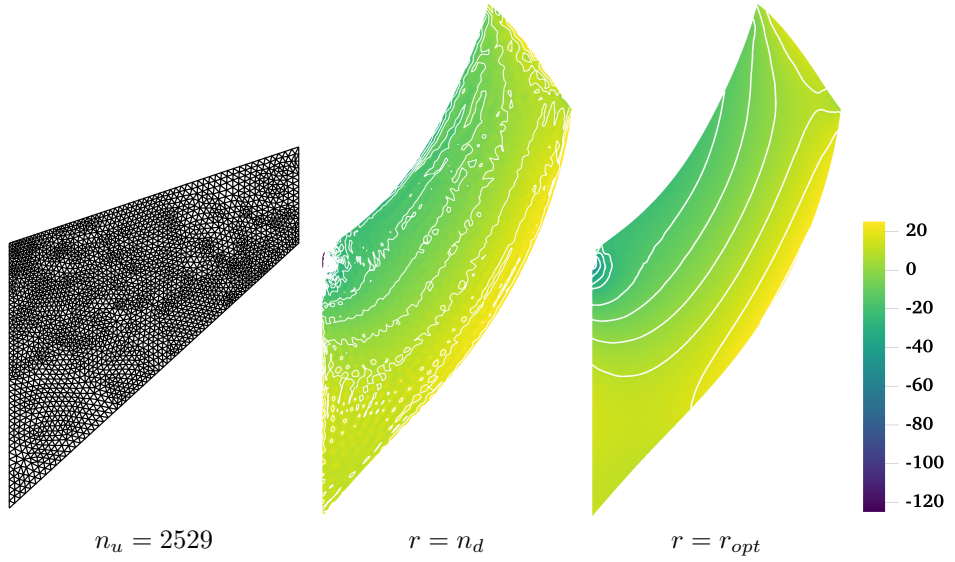


Figure 19: Pressure contour plots for Cook's membrane problem using Tri3-RK

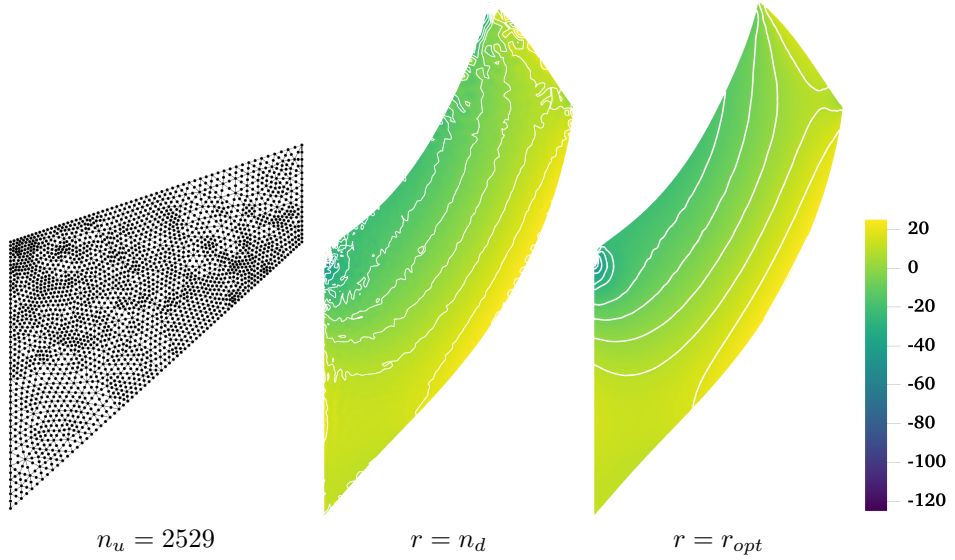


Figure 20: Comparison of pressure contour plots for Cook's membrane problem using Tri6–RK

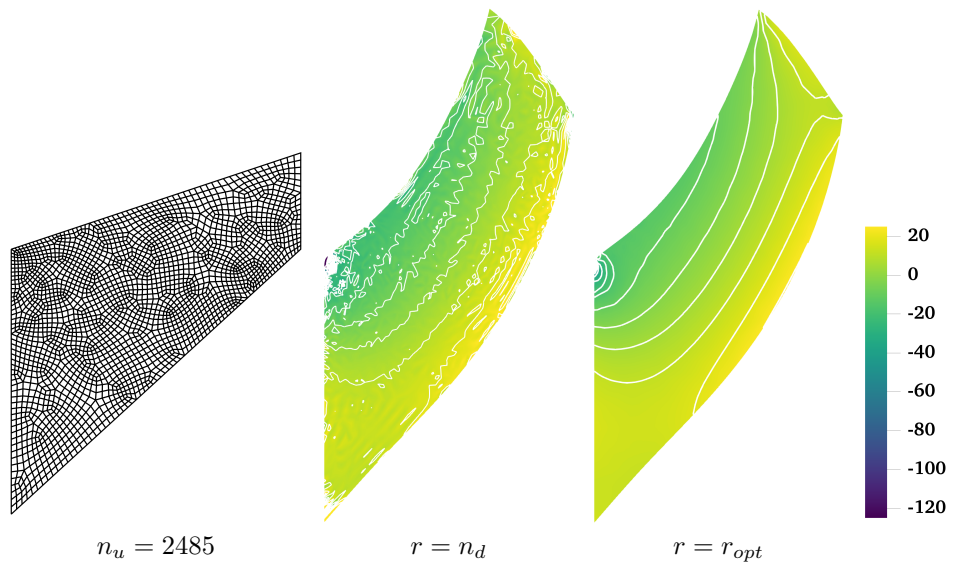


Figure 21: Comparison of pressure contour plots for Cook's membrane problem using Quad4–RK

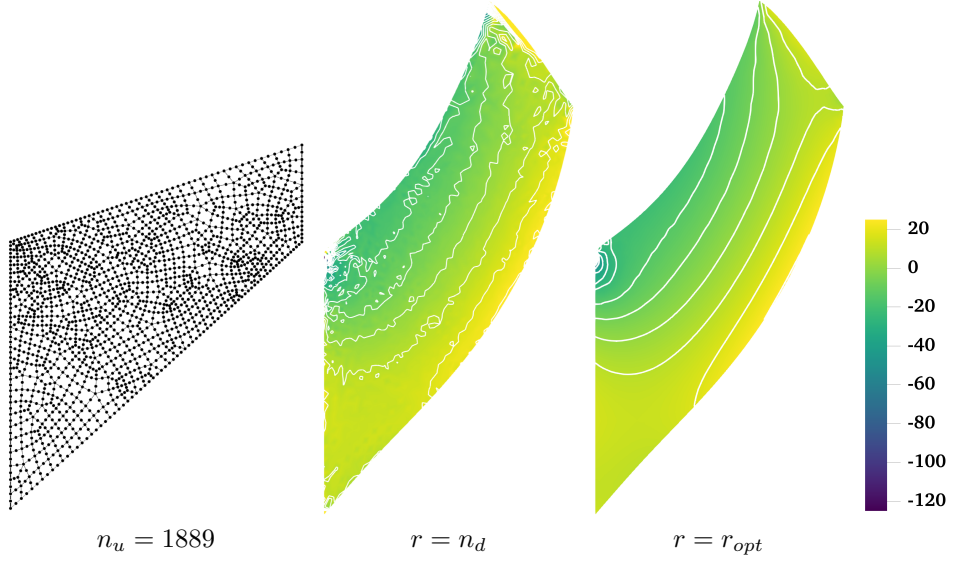


Figure 22: Comparison of pressure contour plots for Cook's membrane problem using Quad8–RK

472 *5.4. Block under compression problem*

473 The incompressible block problem [62] shown in Figure 23 is considered for
 474 testing 3D mixed formulations. The block's dimensions are $2L \times 2L \times L$, $L = 1$.
 475 At the center of the top surface of the block is applied a pressure load P with
 476 the area of $L \times L$. Due to the symmetry of this problem, only a quarter model is
 477 considered. The Young's modulus and Poisson's ratio are set as $E = 240.56839$
 478 and $\nu = 0.5 - 10^{-8}$, respectively.

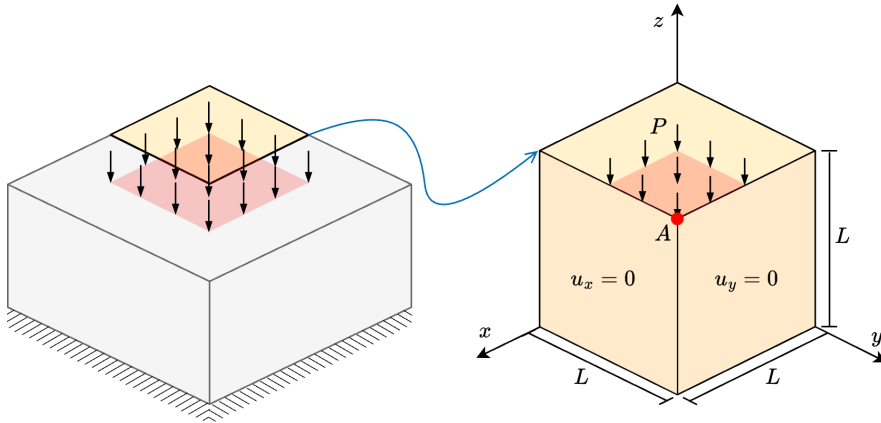


Figure 23: Illustration of block under compression problem

479 The convergence properties of the mixed formulations are evaluated by com-
 480 paring the compression level at point A under various loading conditions P/P_0 ,
 481 where $P_0 = 4$. As shown in Figure 24, all the results exhibit good conver-
 482 gence behavior across different loading levels. Figures 25, 26 study the pressure
 483 stability of 3D mixed FE-meshfree formulations, Tet4-RK and Hex8-RK, with
 484 non-uniform nodal distribution, while the pressure is discretized by linear mesh-
 485 free approximations with a characterized support size of 1.5. The corresponding
 486 results also show the well performance of the proposed optimal constraint ratio
 487 $r = r_{opt}$. The mixed formulations with the traditional constraint ratio $r = n_d$
 488 show comparable displacement results, but exhibit significant pressure instabil-
 489 ity.

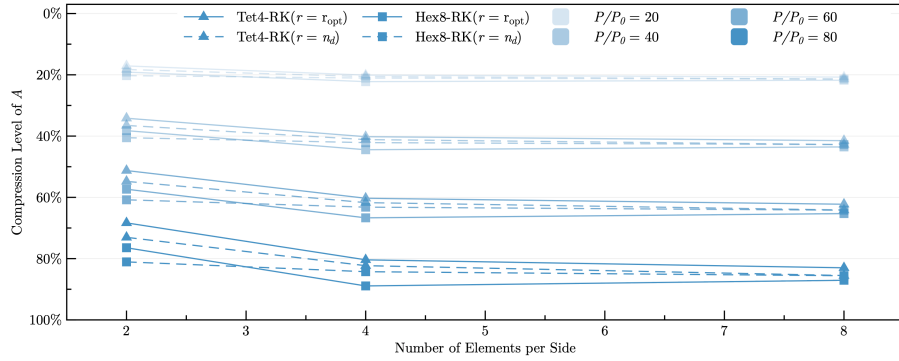


Figure 24: Convergence comparison of compression level (%) at point A for block under compression problem

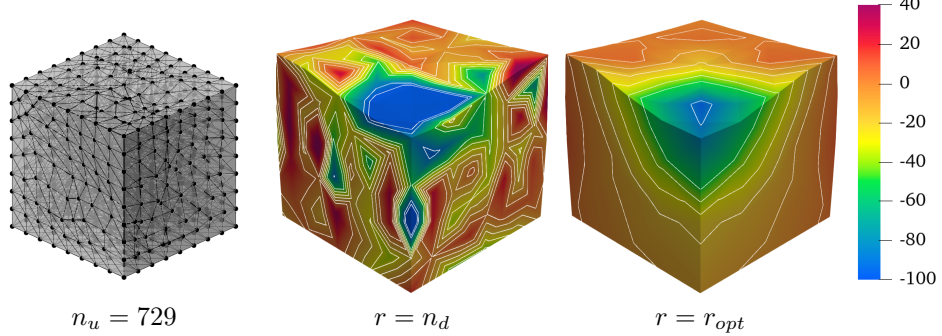


Figure 25: Comparison of pressure contour plots for block under compression problem using Tet4-RK

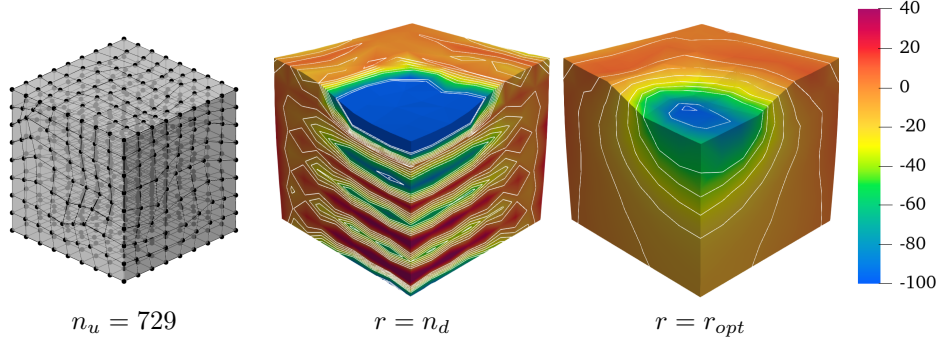


Figure 26: Comparison of pressure contour plots for block under compression problem using Hex8–RK

490 6. Conclusion

491 This paper proposes a novel optimal constraint ratio derived from the inf–sup
 492 condition to address volumetric locking. The optimal constraint ratio requires
 493 that, for a given number of displacement DOFs, the number of pressure DOFs
 494 should remain below a stabilized number determined by the proposed inf–sup
 495 value estimator. For a well-posed nodal distribution, simply counting the dis-
 496 placement and pressure DOFs can determine whether the formulation satisfies
 497 the inf–sup condition. Compared to the traditional constraint ratio, the pro-
 498 posed ratio is theoretically grounded in the inf–sup condition and thus is more
 499 precise.

500 To implement this constraint ratio, a mixed finite element (FE) and meshfree
 501 formulation is developed. Displacements are discretized using 3-node and 6-node
 502 triangular elements, 4-node and 8-node quadrilateral elements in 2D, and 4-node
 503 tetrahedral and 8-node hexahedral elements in 3D. Correspondingly, linear and
 504 quadratic reproducing kernel meshfree approximations are used for pressure
 505 discretization. The reproducing kernel approximation equips globally smooth
 506 shape functions, allowing arbitrary pressure DOF placement without the limit
 507 of element.

508 Inf–sup tests for mixed FE–meshfree formulations with different constraint
 509 ratios verify the effectiveness of the proposed inf–sup value estimator. For effi-
 510 ciency and ease of implementation, the final nodal distribution scheme selects
 511 every other displacement node as a pressure node, ensuring the optimal con-
 512 straint ratio and satisfying the inf–sup condition.

513 A series of 2D and 3D incompressible elasticity examples demonstrate the
 514 effectiveness of the proposed mixed formulation. Results show that formulations
 515 with the optimal constraint ratio yield accurate displacement and pressure solu-
 516 tions. When the constraint ratio exceeds the optimal value, errors rise sharply
 517 to unacceptable levels, with the 8-node quadrilateral element being the only
 518 exception that maintains good displacement accuracy. Error convergence stud-
 519 ies and pressure contour plots further confirm that mixed formulations with

520 the optimal constraint ratio achieve optimal convergence rates and effectively
521 suppress pressure oscillations.

522 **Acknowledgment**

523 The support of this work by the National Natural Science Foundation of
524 China (12102138), the Natural Science Foundation of Fujian Province of China
525 (2023J01108) and the Fundamental Research Funds of Central Universities
526 (ZQN-1014) is gratefully acknowledged.

527 **References**

- 528 [1] F. Brezzi, M. Fortin, Mixed and Hybrid Finite Element Methods, Vol. 15 of
529 Springer Series in Computational Mathematics, Springer, New York, NY,
530 1991.
- 531 [2] T. J. Hughes, The Finite Element Method: Linear Static and Dynamic
532 Finite Element Analysis, Prentice Hall, New Jersey, 2000.
- 533 [3] I. Babuška, R. Narasimhan, The Babuška-Brezzi condition and the patch
534 test: An example, Computer Methods in Applied Mechanics and Engineering 140 (1-2) (1997) 183–199.
- 535 [4] K. J. Bathe, Finite Element Procedures, Prentice Hall, Englewood Cliffs,
536 New Jersey, 1996.
- 537 [5] D. S. Malkus, Eigenproblems associated with the discrete LBB condition for
538 incompressible finite elements, International Journal of Engineering Science 19 (10) (1981) 1299–1310.
- 539 [6] D. Chapelle, K. J. Bathe, The inf-sup test, Computers & Structures 47 (4)
540 (1993) 537–545.
- 541 [7] F. Brezzi, K. J. Bathe, Studies of finite element procedures the inf-sup
542 condition equivalent forms and applications.
- 543 [8] D. Gallistl, Rayleigh-Ritz approximation of the inf-sup constant for the
544 divergence, Mathematics of Computation 88 (315) (2019) 73–89.
- 545 [9] P. Hood, C. Taylor, Navier-Stokes equations using mixed interpolation,
546 Finite element methods in flow problems (1974) 121–132.
- 547 [10] D. S. Malkus, T. J. Hughes, Mixed finite element methods - Reduced and
548 selective integration techniques: A unification of concepts, Computer Meth-
549 ods in Applied Mechanics and Engineering 15 (1) (1978) 63–81.
- 550 [11] T. Shilt, R. Deshmukh, J. J. McNamara, P. J. O'Hara, Solution of nearly
551 incompressible field problems using a generalized finite element approach,
552 Computer Methods in Applied Mechanics and Engineering 368 (2020)
553 113165.

- 556 [12] J. C. Simo, M. S. Rifai, A class of mixed assumed strain methods and
 557 the method of incompatible modes, International Journal for Numerical
 558 Methods in Engineering 29 (8) (1990) 1595–1638.
- 559 [13] M. Broccardo, M. Micheloni, P. Krysl, Assumed-deformation gradient finite
 560 elements with nodal integration for nearly incompressible large deformation
 561 analysis, International Journal for Numerical Methods in Engineering 78 (9)
 562 (2009) 1113–1134.
- 563 [14] W. M. Coombs, T. J. Charlton, M. Cortis, C. E. Augarde, Overcoming vol-
 564 umetric locking in material point methods, Computer Methods in Applied
 565 Mechanics and Engineering 333 (2018) 1–21.
- 566 [15] S. Saloustros, M. Cervera, S. Kim, M. Chiumenti, Accurate and locking-free
 567 analysis of beams, plates and shells using solid elements, Computational
 568 Mechanics 67 (2021) 883–914.
- 569 [16] J. Simo, R. Taylor, K. Pister, Variational and projection methods for the
 570 volume constraint in finite deformation elasto-plasticity, Computer Meth-
 571 ods in Applied Mechanics and Engineering 51 (1-3) (1985) 177–208.
- 572 [17] C. R. Dohrmann, P. B. Bochev, A stabilized finite element method for the
 573 Stokes problem based on polynomial pressure projections, International
 574 Journal for Numerical Methods in Fluids 46 (2) (2004) 183–201.
- 575 [18] A. Valverde-González, J. Reinoso, B. Dortdivanlioglu, M. Paggi, Locking
 576 treatment of penalty-based gradient-enhanced damage formulation for fail-
 577 ure of compressible and nearly incompressible hyperelastic materials, Com-
 578 putational Mechanics 72 (2023) 635–662.
- 579 [19] B.-B. Xu, F. Peng, P. Wriggers, Stabilization-free virtual element method
 580 for finite strain applications, Computer Methods in Applied Mechanics and
 581 Engineering 417 (2023) 116555.
- 582 [20] F. S. Liguori, A. Madeo, S. Marfia, G. Garcea, E. Sacco, A stabilization-
 583 free hybrid virtual element formulation for the accurate analysis of 2D
 584 elasto-plastic problems, Computer Methods in Applied Mechanics and En-
 585 gineering 431 (2024) 117281.
- 586 [21] R. Alves de Sousa, R. Natal Jorge, R. Fontes Valente, J. César de Sá, A new
 587 volumetric and shear locking-free 3D enhanced strain element, Engineering
 588 Computations 20 (7) (2003) 896–925.
- 589 [22] K.-J. Bathe, The inf-sup condition and its evaluation for mixed finite ele-
 590 ment methods, Computers & Structures 79 (2) (2001) 243–252.
- 591 [23] T. J. R. Hughes, Multiscale phenomena: Green's functions, the Dirichlet-
 592 to-Neumann formulation, subgrid scale models, bubbles and the origins of
 593 stabilized methods, Computer Methods in Applied Mechanics and Engi-
 594 neering 127 (1) (1995) 387–401.

- 595 [24] R. Rossi, R. Zorrilla, R. Codina, A stabilised displacement-volumetric
 596 strain formulation for nearly incompressible and anisotropic materials,
 597 Computer Methods in Applied Mechanics and Engineering 377 (2021)
 598 113701.
- 599 [25] E. Karabelas, M. A. F. Gsell, G. Haase, G. Plank, C. M. Augustin, An
 600 accurate, robust, and efficient finite element framework with applications to
 601 anisotropic, nearly and fully incompressible elasticity, Computer Methods
 602 in Applied Mechanics and Engineering 394 (2022) 114887.
- 603 [26] R. Codina, I. Castañar, J. Baiges, Finite element approximation of stabi-
 604 lized mixed models in finite strain hyperelasticity involving displacements
 605 and stresses and/or pressure—An overview of alternatives, International
 606 Journal for Numerical Methods in Engineering (2024) e7540.
- 607 [27] L. Moreno, R. Wuechner, A. Larese, A mixed stabilized MPM formula-
 608 tion for incompressible hyperelastic materials using Variational Subgrid-
 609 Scales, Computer Methods in Applied Mechanics and Engineering 435
 610 (2025) 117621.
- 611 [28] T. J. R. Hughes, L. P. Franca, M. Balestra, A new finite element formu-
 612 lation for computational fluid dynamics: V. Circumventing the babuška-
 613 brezzi condition: A stable Petrov-Galerkin formulation of the stokes prob-
 614 lem accommodating equal-order interpolations, Computer Methods in Ap-
 615 plied Mechanics and Engineering 59 (1) (1986) 85–99.
- 616 [29] A. N. Brooks, T. J. R. Hughes, Streamline upwind/Petrov-Galerkin formu-
 617 lations for convection dominated flows with particular emphasis on the in-
 618 compressible Navier-Stokes equations, Computer Methods in Applied Me-
 619 chanics and Engineering 32 (1) (1982) 199–259.
- 620 [30] L. He, L. Jing, M. Feng, New stabilized mixed finite element methods for
 621 two-field poroelasticity with low permeability, Applied Mathematics and
 622 Computation 494 (2025) 129285.
- 623 [31] D. N. Arnold, F. Brezzi, M. Fortin, A stable finite element for the Stokes
 624 equations, CALCOLO 21 (4) (1984) 337–344.
- 625 [32] F. Auricchio, L. Beirão da Veiga, C. Lovadina, A. Reali, A stability study of
 626 some mixed finite elements for large deformation elasticity problems, Com-
 627 puter Methods in Applied Mechanics and Engineering 194 (9-11) (2005)
 628 1075–1092.
- 629 [33] A. Quarteroni, A. Valli, Numerical Approximation of Partial Differen-
 630 tial Equations, Springer Series in Computational Mathematics, Springer,
 631 Berlin, 1994.
- 632 [34] M. Crouzeix, P. Raviart, Conforming and nonconforming finite ele-
 633 ment methods for solving the stationary Stokes equations I, Revue

- 634 fran aise d'automatique informatique recherche op ationnelle. Math matique 7 (R3) (1973) 33 75.
 635
- 636 [35] U. Brink, E. Stein, On some mixed finite element methods for incompressible and nearly incompressible finite elasticity, Computational Mechanics 19 (1) (1996) 105 119.
 637
 638
- 639 [36] T. Belytschko, Y. Y. Lu, L. Gu, Element-free Galerkin methods, International Journal for Numerical Methods in Engineering 37 (2) (1994) 229 256.
 640
- 641 [37] W. K. Liu, S. Jun, Y. F. Zhang, Reproducing kernel particle methods, International Journal for Numerical Methods in Fluids 20 (8-9) (1995) 1081 1106.
 642
 643
- 644 [38] C. Rodriguez, T.-H. Huang, A variationally consistent reproducing kernel enhanced material point method and its applications to incompressible materials, Computational Mechanics (2023) 1 20.
 645
 646
- 647 [39] S. W. Chi, J. S. Chen, H. Y. Hu, A weighted collocation on the strong form with mixed radial basis approximations for incompressible linear elasticity, Computational Mechanics 53 (2) (2014) 309 324.
 648
 649
- 650 [40] L. Wang, Z. Qian, Y. Zhou, Y. Peng, A weighted meshfree collocation method for incompressible flows using radial basis functions, Journal of Computational Physics 401 (2020) 108964.
 651
 652
- 653 [41] A. Ortiz-Bernardin, M. Puso, N. Sukumar, Improved robustness for nearly-incompressible large deformation meshfree simulations on Delaunay tessellations, Computer Methods in Applied Mechanics and Engineering 293 (2015) 348 374.
 654
 655
- 656 [42] T. J. Hughes, J. A. Cottrell, Y. Bazilevs, Isogeometric analysis: CAD, finite elements, NURBS, exact geometry and mesh refinement, Computer Methods in Applied Mechanics and Engineering 194 (39-41) (2005) 4135 4195.
 657
 658
- 659 [43] F. Auricchio, L. Beir o da Veiga, C. Lovadina, A. Reali, The importance of the exact satisfaction of the incompressibility constraint in nonlinear elasticity: Mixed FEMs versus NURBS-based approximations, Computer Methods in Applied Mechanics and Engineering 199 (5) (2010) 314 323.
 660
 661
- 662 [44] A. Huerta, S. Fern andez-M ndez, Locking in the incompressible limit for the element-free Galerkin method, International Journal for Numerical Methods in Engineering 51 (11) (2001) 1361 1383.
 663
 664
- 665 [45] J. Dolbow, T. Belytschko, Volumetric locking in the element free Galerkin method, International Journal for Numerical Methods in Engineering 46 (6) (1999) 925 942.
 666
 667

- 671 [46] G. Moutsanidis, J. J. Koester, M. R. Tupek, J.-S. Chen, Y. Bazilevs, Treatment
 672 of near-incompressibility in meshfree and immersed-particle methods,
 673 *Computational Particle Mechanics* 7 (2) (2020) 309–327.
- 674 [47] G. Moutsanidis, W. Li, Y. Bazilevs, Reduced quadrature for FEM, IGA
 675 and meshfree methods, *Computer Methods in Applied Mechanics and En-*
 676 *gineering* 373 (2021) 113521.
- 677 [48] Z.-Y. Wang, Y.-F. Jin, Z.-Y. Yin, Y.-Z. Wang, Overcoming volumetric
 678 locking in stable node-based smoothed particle finite element method with
 679 cubic bubble function and selective integration, *International Journal for*
 680 *Numerical Methods in Engineering* 123 (24) (2022) 6148–6169.
- 681 [49] T. Elguedj, Y. Bazilevs, V. Calo, T. Hughes, B^- and F^- projection meth-
 682 ods for nearly incompressible linear and non-linear elasticity and plasticity
 683 using higher-order NURBS elements, *Computer Methods in Applied Me-*
 684 *chanics and Engineering* 197 (33-40) (2008) 2732–2762.
- 685 [50] J. S. Chen, S. Yoon, H. P. Wang, W. K. Liu, An improved reproducing
 686 kernel particle method for nearly incompressible finite elasticity, *Computer*
 687 *Methods in Applied Mechanics and Engineering* 181 (1) (2000) 117–145.
- 688 [51] C. M. Goh, P. M. F. Nielsen, M. P. Nash, A stabilised mixed mesh-
 689 free method for incompressible media: Application to linear elasticity and
 690 Stokes flow, *Computer Methods in Applied Mechanics and Engineering* 329
 691 (2018) 575–598.
- 692 [52] D. S. Bombarde, M. Agrawal, S. S. Gautam, A. Nandy, Hellinger–Reissner
 693 principle based stress–displacement formulation for three-dimensional iso-
 694 geometric analysis in linear elasticity, *Computer Methods in Applied Me-*
 695 *chanics and Engineering* 394 (2022) 114920.
- 696 [53] H. Casquero, M. Golestanian, Vanquishing volumetric locking in quadratic
 697 NURBS-based discretizations of nearly-incompressible linear elasticity:
 698 CAS elements, *Computational Mechanics* 73 (6) (2024) 1241–1252.
- 699 [54] A. Huerta, Y. Vidal, P. Villon, Pseudo-divergence-free element free
 700 Galerkin method for incompressible fluid flow, *Computer Methods in Ap-*
 701 *plied Mechanics and Engineering* 193 (12-14) (2004) 1119–1136.
- 702 [55] C. T. Wu, W. Hu, J. S. Chen, A meshfree-enriched finite element method
 703 for compressible and near-incompressible elasticity, *International Journal*
 704 *for Numerical Methods in Engineering* 90 (7) (2012) 882–914.
- 705 [56] T. Vu-Huu, C. Le-Thanh, H. Nguyen-Xuan, M. Abdel-Wahab, A high-
 706 order mixed polygonal finite element for incompressible Stokes flow analy-
 707 sis, *Computer Methods in Applied Mechanics and Engineering* 356 (2019)
 708 175–198.

- 709 [57] E. Stein, R. de Borst, T. J. R. Hughes (Eds.), Encyclopedia of Computational Mechanics, John Wiley, Chichester, West Sussex, 2004.
- 710
- 711 [58] I. Babuška, J. Osborn, Eigenvalue Problems, in: Handbook of Numerical Analysis, Vol. 2 of Finite Element Methods (Part 1), Elsevier, 1991, pp. 712 641–787.
- 713
- 714 [59] K. Yosida, Functional Analysis, 6th Edition, Classics in Mathematics, Springer-Verlag, Berlin Heidelberg, 1995.
- 715
- 716 [60] J. Wu, D. Wang, An accuracy analysis of Galerkin meshfree methods ac-
717 counting for numerical integration, Computer Methods in Applied Mechan-
718 ics and Engineering 375 (2021) 113631.
- 719
- 720 [61] S. Timoshenko, J. Goodier, Theory of Elasticity, Engineering Mechanics Series, McGraw-Hill, 1969.
- 721
- 722 [62] S. Reese, P. Wriggers, B. D. Reddy, A new locking-free brick element tech-
723 nique for large deformation problems in elasticity, Computers & Structures
75 (3) (2000) 291–304.
- 724